ANALYSIS OF PACIFIC HOTSPOT CHAINS AND A MODEL FOR RECENT PLUME DRIFT

A THESIS SUBMITTED TO THE GRADUATE DIVISION OF THE UNIVERSITY OF HAWAIʻI AT MĀNOA IN PARTIAL FULFILLMENT OF THE REQUIREMENTS FOR THE DEGREE OF

MASTER OF SCIENCE

IN

EARTH AND PLANETARY SCIENCES

AUGUST 2021

By

Andrew A. Chase

Thesis Committee:

Paul Wessel, Chairperson
L. Neil Frazer
Jasper G. Konter

ABSTRACT

Age-progressive seamount trails created by long-lived deep-mantle plumes have been used to establish absolute reference frames for plate motion. However, when plume drift is considered, changes in seamount trail direction and age progression rate cannot be attributed to plate motion change alone. A better understanding of these absolute motions are needed for studying the mantle dynamic processes that drive both plate tectonics and plume drift. For this study, improvements to age-progressive curves of eleven Pacific hotspot chains are made independently of past plate motion models. Our approach involves bathymetry processing to robustly predict a smooth and continuous hotspot path by connecting high points in seamount bathymetry, with uncertainties in the path based on seamount trail width and amplitude. Ages found using radiometric dating techniques from seamount samples are projected onto the inferred hotspot trail. A best-fit model of age as a function of along-track distance is determined, giving continuous age progressions for each seamount chain with uncertainties in both age and path. Three different types of paleolatitudes are also examined by incorporating data from the magnetization of seamount drill core samples, paleo-poles from marine magnetic anomaly skewness, and paleo-spin-axes from shifts in equatorial sediments. Improved paleolatitude curves for the Hawaiian-Emperor and Louisville chains are determined by combining these three different types of data. Paleolatitude curves are also determined for other chains where a sufficient amount of paleo-pole or paleo-spin-axis data are available. The data analysis of these eleven Pacific seamount chains provide prime constraints for future plate and plume motion models. For this study, we examine the data by accessing the change over time in distance between coeval seamounts, which infers relative drifts between the hotspots at different times in the past. We find that the inter-hotspot distance change since 6 Ma have been linear, given the (relatively large) errors, which prompted the development of a novel modeling approach. We end with inverting these linear relative rates via our new modeling scheme and solve for recent plume drifts for the time frame of 6 Ma to the present.

CONTENTS

LIST OF TABLES

LIST OF FIGURES

CHAPTER 1
INTRODUCTION

In the study of plate tectonics, the hypothesis of deep-mantle plumes giving rise to hotspots at the surface (Wilson 1963) has been used to establish absolute reference frames for plate motion. With the initial assumption of fixed mantle plumes, changes in seamount trail geometries were directly attributed to changes in plate motion. For instance, Morgan (1971) interpreted the ~120 degree bend in the Hawaiian-Emperor seamount chain as a major change in Pacific plate motion sometime between ~40–50 Ma. Numerous absolute plate motion (APM) models have been derived from these assumptions (e.g. Duncan and Clague 1985; Koppers et al. 2001; Wessel and Kroenke 2008). However, not long after the idea of using hotspot trails to infer absolute plate motions was introduced, the very fixity of hotspots was questioned (e.g. Winterer 1973). Furthermore, early laboratory experiments demonstrated that plume conduits can be deflected laterally on their way to the surface from background mantle flow (e.g. Skilbeck and Whitehead 1978). Later, mantle flow models were used to predict plume drifts that could be compared with plate reconstruction models and seamount trail geometries (e.g. Steinberger 2000). Early paleolatitude data also provided hints at latitudinal shifts (e.g. Kono 1980) by looking at the magnetization of rock samples, revealing the magnetic field inclination at the time of seamount formation. Further studies have since strengthened this line of reasoning (e.g. Tarduno and Cottrell 1997; Tarduno et al. 2003; Tarduno et al. 2009; Bono et al. 2019). Without the assumption of hotspot fixity, changes in seamount trail geometries and age progressions must reflect a combination of plate and plume motions. While not unique, models seeking to reconcile plate and plume drifts have therefore been proposed (e.g. O'Neill et al. 2005; Doubrovine et al. 2012; Tetley et al. 2019).

The Pacific plate is the largest of the tectonic plates present on Earth today. It is relatively fast-moving and a host to many hotspot chains, making it ideal for studying absolute plate and plume motions. However, without any clear constraint on plume drifts, an accurate plate reconstruction model cannot be determined by seamount chain geometries and ages alone. To what extent plate motion or plume drift influenced these seamount chains is still a debated topic today, most notably regarding the formation of the Hawaiian-Emperor bend (HEB), with recent developments coming to very different conclusions. For instance, Torsvik et al. (2017) argued that the plume drift needed to form the bend without a major change in plate motion would not be consistent with mantle flow models, while Bono et al. (2019) argued that paleolatitude and inter-hotspot separations between the Hawaiian-Emperor and Louisville chains are consistent with a rapid southward drift of the Hawaiian hotspot during the formation of the Emperor seamounts. Finally, Woodworth and Gordon (2018) argued for major plate reorganizations with much of the paleolatitude data better explained by true polar wander (e.g. Goldreich and Toomre 1969; Tsai and Stevenson 2007). With

1

this major unresolved problem in the field of plate tectonics, further study in the Pacific region is needed to bring clarity to the issue. In this paper, we explore a more robust analysis of Pacific seamount chain data with the aim of adding specific constraints on models for both plate and plume drifts.

For this study, we examined data from eleven Pacific hotspot chains. These chains are (with abbreviations in parenthesis), Hawaiian-Emperor (HI), Louisville (LV), Rurutu (RU), Cobb (CB), Kodiak (KO), Foundation (FD), Pitcairn (PC), Samoa (SA), Caroline (CR), Marquesas (MQ), and Society Islands (SO). We use a robust model-independent approach for their analysis. The data sets considered include seamount bathymetry (to constrain geometry), radiometric age samples (to constrain age progressions), paleolatitudes from the magnetization of rock samples, paleo-poles from marine magnetic anomaly skewness and paleo-spin-axes from equatorial sediment shifts (to constrain latitudinal plume drifts). A summary of all these data sets is displayed in **Figure 1.1**. Out of the eleven hotspot chains, three have recorded ages older than the ~ 50 Ma HEB (i.e., HI, LV, and RU) and six are long-lived enough to allow us to infer paleolatitudes from coeval paleo-poles and spin-axis-poles (i.e., HI, LV, RU, CB, KO, and FD). With these data, we present objective and reproducible approaches to their analysis that provide prime constraints for future modeling seeking to separate plate motions from plume drifts. We end with an analysis of the data and our preliminary inferences for plume drift during the last 6 Myr.
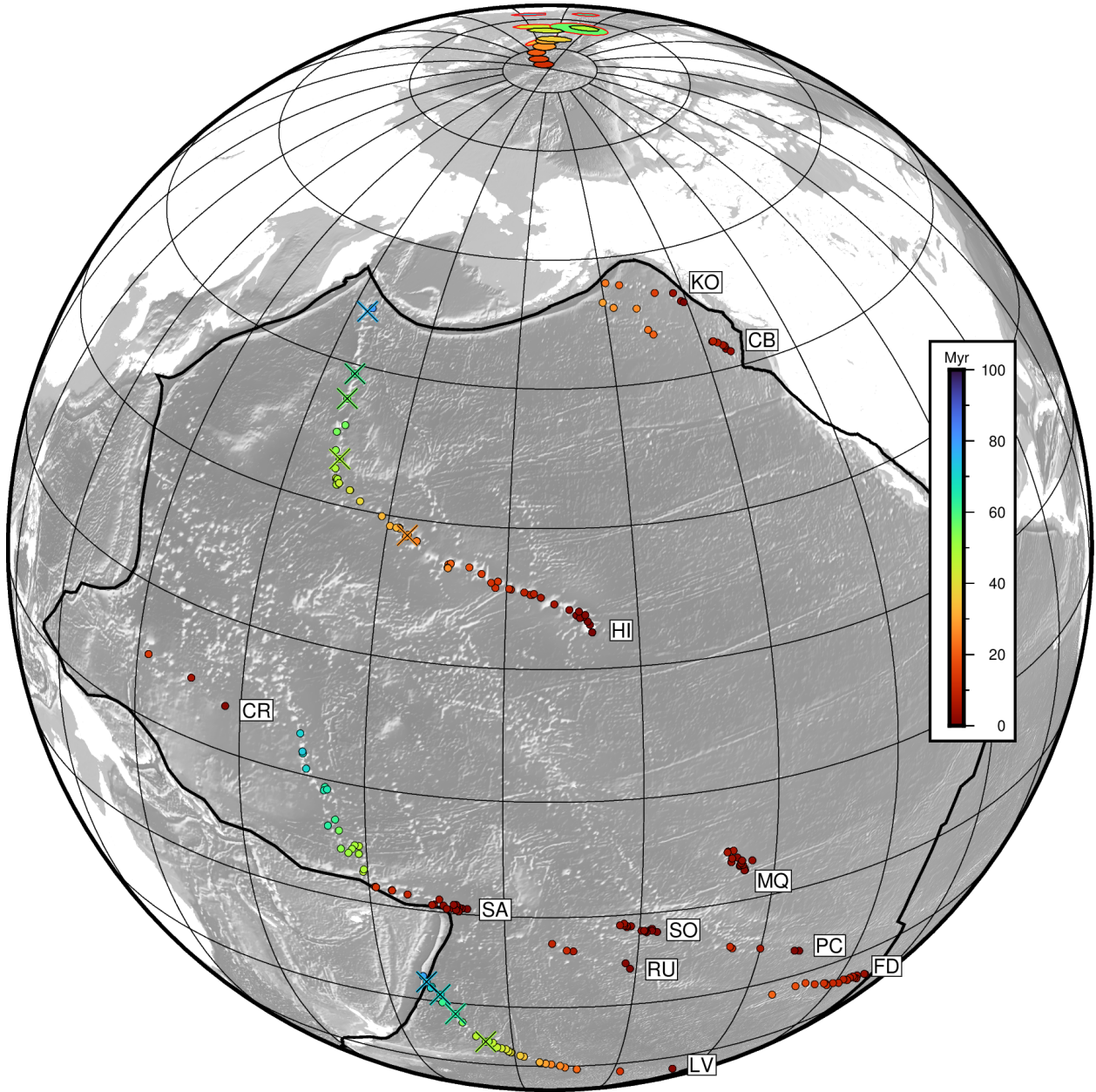
Figure 1.1: Summary of all data examined for this study. A grey-scale bathymetry grid of the Pacific region is displayed with the Pacific plate boundaries (thick black line). Radiometric age data for all eleven chains are displayed (colored circles) as well as rock magnetization samples (colored crosses), paleo-magnetic poles (red-outlined ellipses) and paleo-spin-axes (black-outlined ellipses). Age data, rock magnetization, and paleo-poles all follow the same color scale.

CHAPTER 2
DATA ANALYSIS

2.1   Preparing Residual Bathymetry

In order to determine hotspot trail geometries, the seamounts that make up a chain are separated from other seafloor features. To achieve this separation objectively, a balancing act must be performed to remove as many unrelated features as possible while not removing the data of interest, in this case the seamounts formed from the eleven hotspots.

Starting with a raw bathymetry grid of the Pacific region (Tozer et al. 2019) shown in **Figure 2.1a**, both seafloor subsidence (Müller et al. 2019; Hillier and Watts 2005) and sediment thickness corrections (Whittaker et al. 2013) were applied. To further reduce the impact of long-wavelength features on the ocean floor, a robust filtering scheme was used based on the regional-residual separation methodology of Wessel (1998; 2016). The process involves using a median filter to eliminate large length-scale bathymetric features (e.g., swells and oceanic plateaus), smoothing the median-filtered grid with a secondary Gaussian filter to suppress minor artifacts left behind by the median filter, and subtracting the resulting regional trend from the corrected seafloor. While this method works to objectively and reproducibly remove unrelated features from the data, a few subjective decisions had to be made throughout the process. One such decision included masking out large bathymetric features in close proximity to seamount chains that otherwise would skew the filter process. These features include (with abbreviations in parenthesis) the Hess Rise (HR), Hikurangi Plateau (HP), Manihiki Plateau (MP), Mid-Pacific Mountains (MM), Ontong Java Plateau (OP), and Shatsky Rise (SR) (**Figure 2.1b**).

The filter radius determines which features will remain or be removed once the regional trend is subtracted from the seafloor. Wessel (2016) found that on average, a filter full width (6 sigma) of 420 km worked well for the Hawaiian chain. However, with seamount chains differing by size and superimposed on a highly variable seafloor morphology, using a single filter width for the entire Pacific seafloor will not be successful for all chains. To account for this variability we used a filter of varying size based on an estimated age of the seafloor when seamount loading occurred, effectively following a square-root of age curve (see **Appendix A.1**) designed to dampen the flexural wavelengths associated with lithospheric deformation (e.g. Watts 2001). For example, the filter around the Hawaiian-Emperor chain was wider toward the south-east where the seamounts were loaded on older crust (e.g., 80–90 Myr), becoming progressively narrower as it worked its way up the Emperor chain. This fine-tuning allowed the filter to better capture and isolate seamounts whose nearby seafloor is more effected by plate flexure. However, this method needed adjusting for the Emperor

and Samoa chains because of their close proximity to a subduction zone. For the Emperor chain, a minimum filter width of 380 km was assigned and for Samoa a constant filter width of 420 km was used.

Each chain is encompassed by its own envelope drawn to comfortably include all seamounts in the chain (**Figure 2.1c**). However, after corrections and filtering, smaller unrelated features still remain within the envelopes (e.g., abyssal hill fabric or smaller, near-ridge seamounts unrelated to hotspot formation). To further reduce these features, a base contour was applied, allowing us to remove any features below the threshold. To determine an appropriate contour threshold, the mean height (i.e., the ratio of volume over surface area) for each residual seamount chain as a function of contour interval was examined. While there was no clear or unique inflection point in the relationship between mean height and contour values, the 500 m contour was chosen based on a slight leveling off of mean height for that threshold as well as a visual inspection of the chains viewed at a range of contour values. With these adjustments, the final residual bathymetry grid was obtained (**Figure 2.1d**).

2.2   Inferred Hotspot Trails

Rather than relying on predicted paths from past APM models or tracing lines through the seamounts by eye to infer the hotspot paths, an objective method is desired. The residual bathymetry of each seamount chain determined by the methods outlined in **Section 2.1** was used to determine these paths. A 700 km full width 2D Gaussian filter was applied to smooth the residual grid. This method of filtering differs from that used in **Section 2.1** which sought to find and separate the regional trend from the data, whereas here we chose to smooth the residual data and directly use the result for determining our medial trail line. A smoothed bathymetry is desired because inferring a hotspot trail using the raw seamounts creates a jagged line that is oscillating with distance at wavelengths much too short for the resolutions we can predict, given the likely spatial and temporal scales of plume-plate interactions (e.g. Ballmer et al. 2013). Next, a subjectively drawn starting line that reasonably follows the peaks of the non-smoothed seamounts (**Figure 2.2a**) was used to record perpendicular cross-profiles every 20 km along it (**Figure 2.2b**). With our starting line and its perpendicular cross-sections of the smoothed bathymetry of the chains, we identified the peak along the smoothed bathymetry for each cross-section and used these locations as revised center points to infer a new hotspot path (**Figure 2.2c**) and its uncertainty (**Figure 2.2d**). An example in cross-section view is shown in **Figure 2.3**.

This approach works best for seamount chains with significant data coverage throughout the entirety of the chain. However, some chains, e.g., LV and RU, have large gaps between some seamounts with little to no intervening data. These gaps create unrealistic excursions and discontinuities along
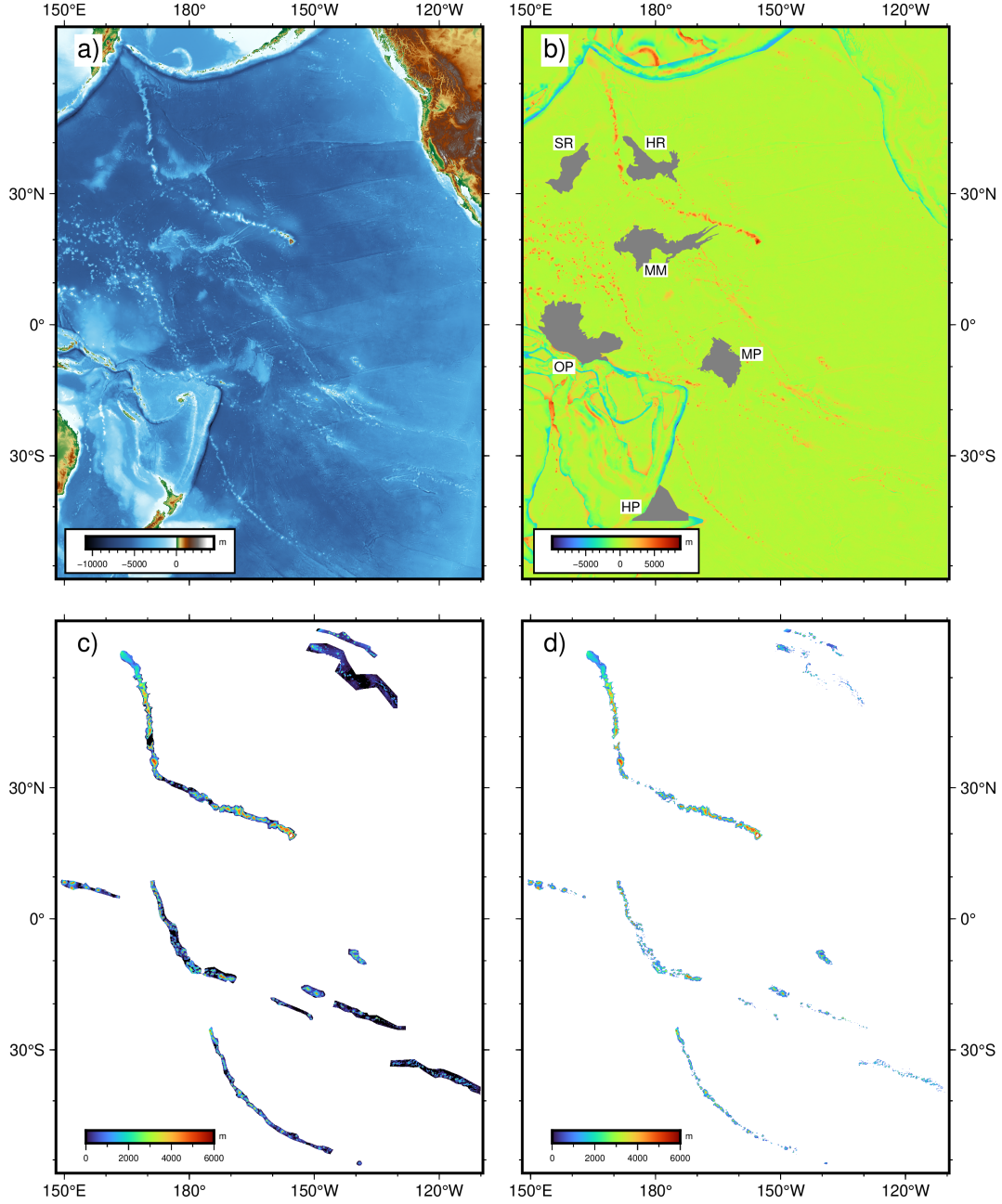
Figure 2.1: Bathymetry grids of the Pacific region showing all eleven seamount chains. (a) Raw relief data from Tozer et al. (2019) . (b) Result after applying seafloor subsidence and sediment thickness correction and subtracting the regional trend found via median and Gaussian filters. For simplicity, the result of a constant 420 km filter width is displayed here, however, a varying filter width unique to each chain was the chosen method for this study. Masks to cover unrelated features are displayed as grey polygons. (c) The residual bathymetry encompassed by each seamount chain envelope. The residual bathymetry shown here is the result of using a varying filter width per chain and not the constant 420 km filter displayed in **Figure 2.1b**. RU and SA are the only chains to have overlapping envelopes. (d) The residual bathymetry after applying a 500 m contour threshold.

the inferred path. To correct for these artifacts, the final estimated path was chosen as a weighted average of the initial and tracked paths, with along-track profile heights used to assign the relative weight. This method is shown in **Figure 2.4**. To further reduce any remaining short-wavelength excursions in the path, a final 1D Gaussian filter was applied to smooth the weighted line. Widths for the 1D Gaussian filters vary by chain, typically with a range of 150–300 km full widths with the exceptions of RU, KO, and CR which have larger filter widths due to their higher age uncertainty. The filter widths for the 1D Gaussian filter were initially set to 300 km but were later revised based on inferences we drew from the along-track age progressions and their uncertainties, to be discussed in **Section 2.3**. In contrast, the 700 km 2D Gaussian filter used to smooth the residual grid was not changed after the inferences from the age progressions.

The geometric analysis of the seamount chains we have presented here is not a completely objective methodology. The use of very different filter widths or contour thresholds would give different medial trails. A different starting line and different sampling intervals for the cross-profiles may also result in slightly different medial trails. However, we explored such variability and found them to be modest. Nevertheless, by quantifying these settings and applying them via clearly described algorithms, the method is reproducible should other parameters be deemed more appropriate after further study.

2.3 Chain Age Progressions

Traditionally, a systematic increase in seamount ages along a hotspot chain has been used as a key observation in support of the modeling of absolute plate motions (e.g. Morgan 1971). In order to provide these modeling constraints, discrete radiometric age data (e.g. Duncan and Clague 1985) must be fit to separate continuous age progression curves for each chain. To achieve this, age samples must be assigned a function of distance along the chain's inferred hotspot path. Therefore, sample locations were projected onto the closest point to the medial line from their actual position. An example of this step for the Hawaiian-Emperor chain can be seen in **Figure 2.5** as well as for the remaining ten chains in **Figure A.1**.

Numerous prior studies have assessed the age progressions along hotspot chains (e.g. Duncan and Clague 1985; Koppers, Gowen, et al. 2011; Koppers, Russell, et al. 2011; Doubrovine et al. 2012; O'Connor et al. 2013; Wessel 2016; Jicha et al. 2018; Wessel and Conrad 2019), often using linear regression or linear splines with knots. In this study, the chosen method for fitting the distance along trail verses age data was a weighted continuous polynomial regression. However, a few steps were taken before the regression was performed. To start, we gathered the most recently available radiometric age data from seamounts on the Pacific plate (i.e. Clouard and Bonneville 2005; Sharp and Clague 2006; Koppers, Gowen, et al. 2011; Koppers, Russell, et al. 2011; O'Connor et al. 2013;
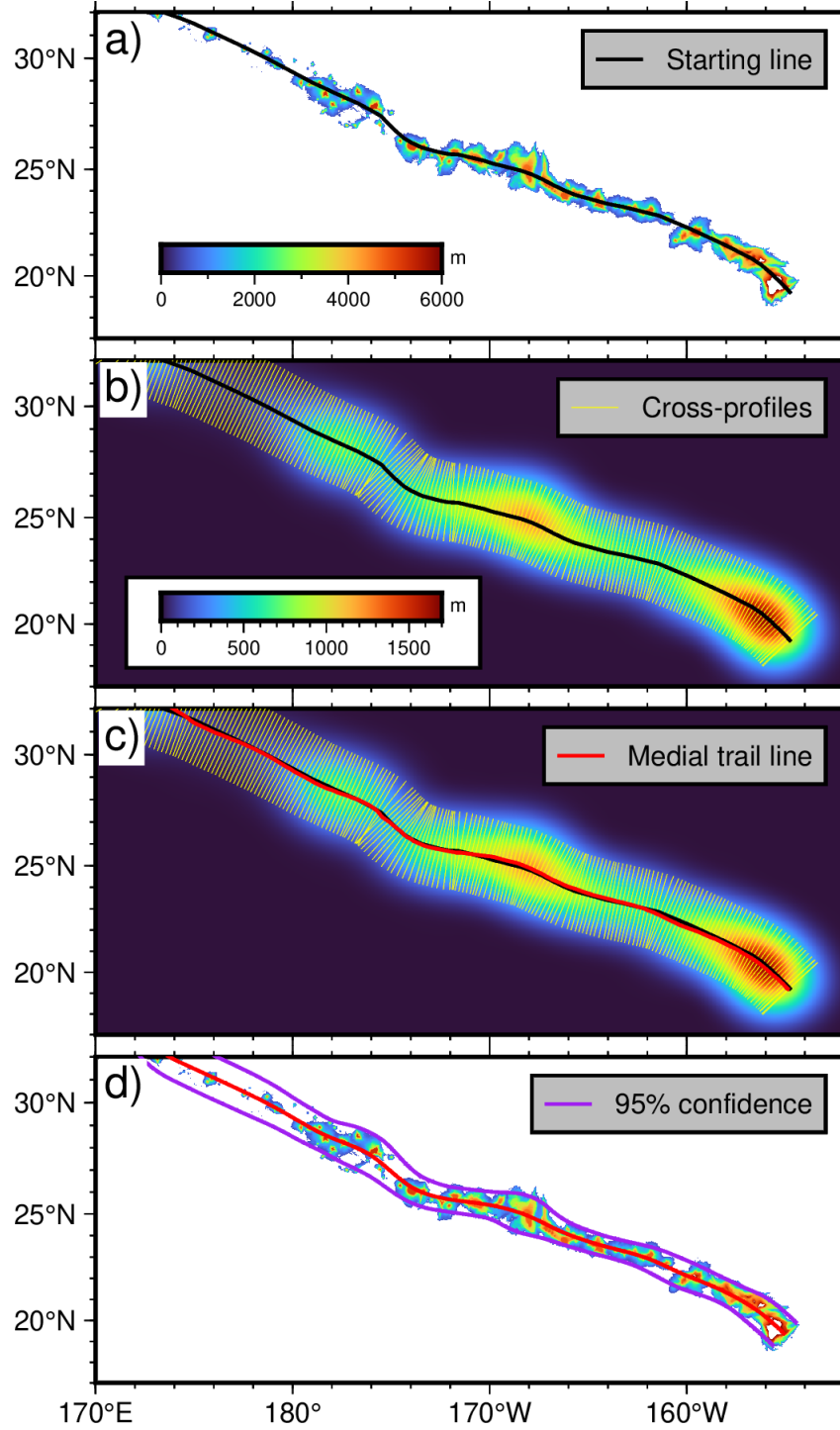
Figure 2.2: Geometric analysis of the south-east Hawaiian chain. (a) Residual bathymetry with the subjectively drawn starting line (black line). (b) Residual bathymetry grid smoothed with a 700 km 2D Gaussian filter. Cross-profiles (yellow line) have a length of 400 km, drawn every 20 km along the chain and sampled every 2 km along each profile. (c) Medial trail line (red line) inferred from connecting high points along the smoothed grid recorded by the cross-profiles. (d) Across-track 95% confidence bands (purple lines) are determined based on seamount width and amplitude.

8
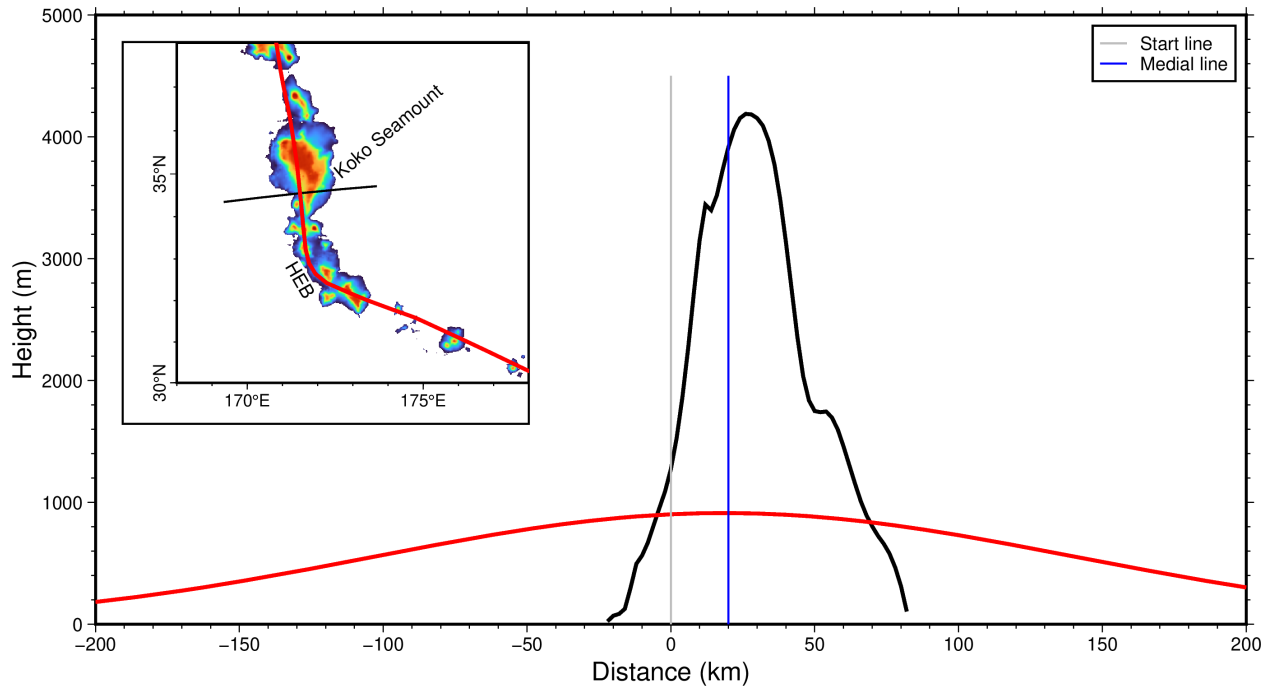
Figure 2.3: Cross-section view through the Koko Seamount which is part of the southern Emperor chain. The cross-section shows both the residual bathymetry (black line) and the smoothed bathymetry (red line) after being processed by the 700 km 2D Gaussian filter. The start line location (grey vertical line at zero distance) is compared to the improved medial point along the cross-section (blue vertical line).
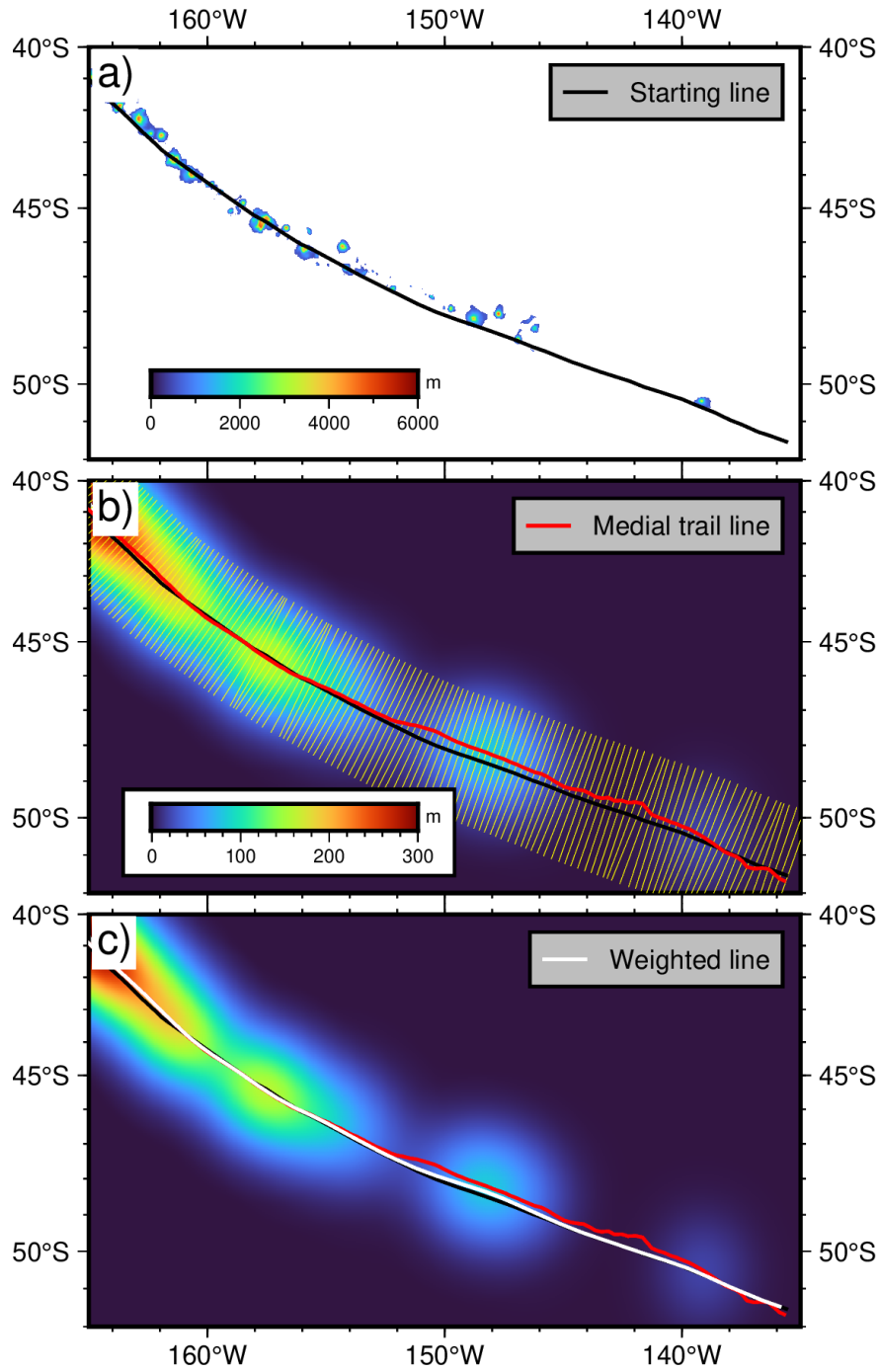
Figure 2.4: Geometric analysis of the south-east Louisville chain. (a) Residual bathymetry of the south-east Louisville chain with the subjectively drawn starting line (black line). (b) Residual bathymetry grid smoothed with a 700 km 2D Gaussian filter. (c) The white line is weighted towards the starting line in areas with little to no data. In areas with sufficient data the weighted line reverts back to the original medial trail line.

Jicha et al. 2018; Konrad et al. 2018; Heaton and Koppers 2019). Next, the data were binned every 50 km along track to avoid the regression favoring sections where large numbers of data are clustered. For the chains LV, RU, and SA, a couple of points were manually binned because of their close proximity to one of the 50 km bin edges. A weighted average and weighted standard deviation determined the binned points' new positions and uncertainties. A non-weighted polynomial regression was then performed on the binned data, with an F-test used to determine the statistically significant polynomial parameter order. The standard deviation of the points along this non-weighted regression was used to assign a minimum value for the uncertainty of each individual data point. The justification for the altering of the measurement errors is that these analytical errors do not properly represent the spread of ages commonly found when one seamount is sampled many times. These small analytical errors can make the weighted regression favor sparser data points with very small measurement errors over binned data representing a spread of many data points. While the analytical precision in sample ages is typically small, each volcano could be active for > 5 Ma (e.g. Koppers, Russell, et al. 2011), so when only sampled one or two times, the sample age does not represent the spread of ages that can be found throughout the island or seamount. Once these new errors are assigned, they were used to determine weights for the final regression curve, where a weighted F-test was performed to determine the polynomial parameter order of the weighted regression model.

Uncertainties from the age curve regressions can be used to determine spatial uncertainties for the along-track hotspot trail. This conversion was done by calculating the inverse of the local slope along the age curves (yielding relative plate speed) and multiplying these rates by the age uncertainty in the curves. For each chain, an average of their one-sigma uncertainty throughout the chain was calculated. The six-sigma averages for each chain gives insight into appropriate filter width sizes used in **Section 2.2**. However, since an inferred hotspot trail is needed to produce the age curves, this process was first done using preliminary hotspot trails using the same filter width sizes for each chain. This exercise gave us an idea of what uncertainties to expect and we thereby altered the filter widths accordingly to come up with the final medial trail lines. These medial trail lines were then used to create the final age progression curves, two examples of which are displayed in **Figure 2.6** with the remaining chains displayed in **Figure A.2**.

One consequence of using this objective methodology for determining a seamount chain age progression is the possibility for inconsistencies between the zero age location determined by the regression fit and what is known (or assumed) to be the true present-day hotspot location. This is most obvious for the Hawaiian hotspot, where the present-day hotspot location is believed to be well known. Our initial second-order polynomial fit for HI failed to properly fit the younger ages, crossing the distance-axis about 100 km up-trail from the known location of the hotspot. Since these younger

ages ($\sim 6-0$ Ma) have big implications in plate tectonics and the results of this study, and since we have a more precise set of data for those ages, we decided to override the results of the regression for HI and use an approach that better fits the data. The new approach taken for HI fits a cubic spline that is split into two segments at 800 km, satisfying continuity of value and the first two derivatives. The resulting curve better fits the young ages as found by Clague (1996) as well.
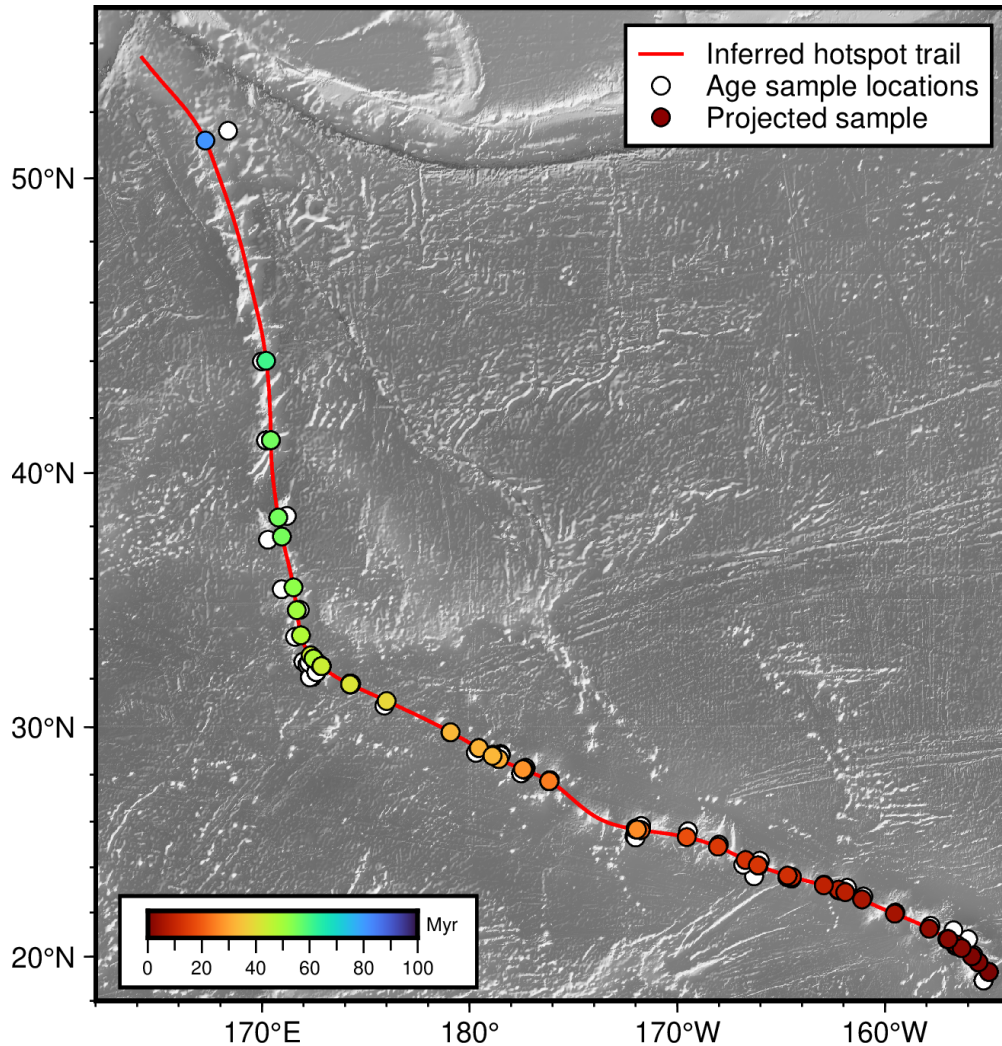
Figure 2.5: Radiometric age sample locations (white circles) for the Hawaiian-Emperor chain, projected onto the inferred medial hotspot trail (red line) and colored according to sample age (colored circles). Plots for the remaining chains are in **Figure A.1**.

2.4   Paleolatitudes

Three different types of data are used to determine a hotspot's latitude at a given time in the past. One data type results from the magnetization of vertically oriented rock samples taken from
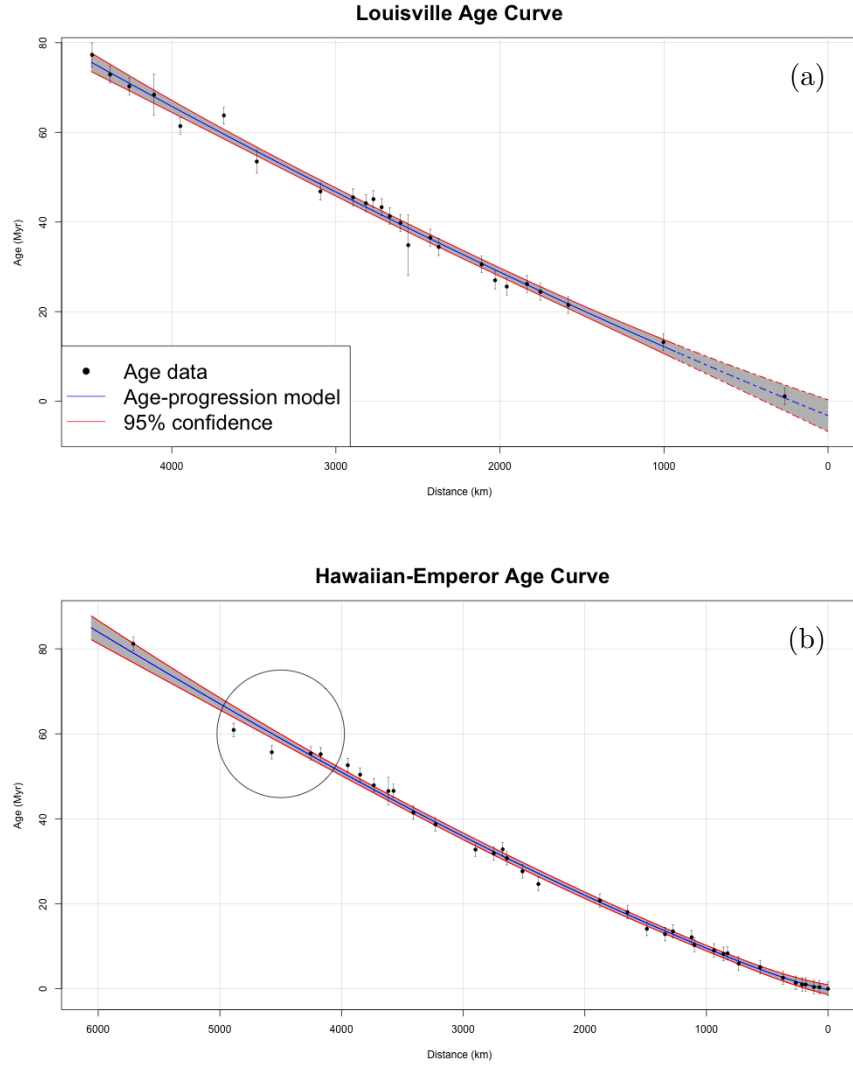
Figure 2.6: Binned radiometric age data from the Hawaiian-Emperor and Louisville chain. (a) The curve for Louisville was fit by a weighted polynomial regression. A weighted F-test was performed to determine the models' parameter order, which for Louisville represents a second-order polynomial fit. The dashed line represents the portion of the chain where there is a large gap with little to no seamount data. (b) The Hawaiian-Emperor chain fit by a split cubic spline at 800 km, which is approximately the middle of the gap between the ~ 6 Ma and ~ 8 Ma data points. The circled points represents an area of data that shows a break from the trend, however, unlike the younger portion of the chain where we have a higher confidence in the age data and therefore split the spline to better fit that section, in the circled section we have less confidence in the data and higher spatial uncertainties and therefore do not alter the trend in that area.

13

seamount drill cores. These samples reveal the magnetic field inclination with respect to magnetic north at the time of formation and therefore the latitude of the hotspot when actively forming the seamount (e.g. Tarduno et al. 2003; Bono et al. 2019), provided the field can be approximated by a geocentric dipole that tracks the spin-axis (Tauxe 2006). This type of data is presently only available for the Hawaiian-Emperor and Louisville seamount chains. Since the samples lack azimuthal orientation, no paleolongitude can be extracted.

Another approach to determine paleolatitudes along a seamount chain is to rely on predicted values based on the paleo-poles derived from marine magnetic anomaly skewness (Cande 1976). From a set of magnetic anomalies crossing the same isochron but at different locations, one can determine a best-fitting paleo-pole for the age of the isochron (e.g. Petronotis et al. 1994). Therefore, a paleo-colatitude for coeval seamounts anywhere on the Pacific plate can be predicted by calculating the angular distance between the paleo-pole and the coeval position along the seamount trail (see **Figure 2.7**).

Similar to the poles inferred from magnetic anomalies, paleo-spin-axes can be inferred by analyzing latitudinal shifts in equatorial sedments. These sediments initially formed at the equator but have since been carried northwards by plate motion (Parés and Moore 2005). Given an age for these displaced sediments, a paleo-spin-axis can be determined (Woodworth and Gordon 2018) and therefore a coeval seamount's paleo-colatitude for any trail on the Pacific plate can be inferred.

A non-weighted continuous polynomial regression was used to fit a data set combining all three types of paleolatitude data. An F-test was performed to determine the models' parameter order, however, in some cases the F-test was overridden because of clear violations to trends in the data. HI, LV, and RU all used a third-order polynomial to describe their fit, while CB, KO, and FD are fitted using linear trends. The latter three chains only contain predicted paleolatitudes derived from the equatorial sediment paleo-spin-axes because they have not yet been sampled for rock magnetization and are too young for any of the anomaly skewness paleo-poles to apply.

Our analysis on paleolatitudes thus far assumes no true polar wander (TPW) has taken place. True polar wander argues that at times in the past there have been re-positionings of Earth's spin-axis (Goldreich and Toomre 1969). For instance, Woodworth and Gordon (2018) proposed an episode of TPW during the time of Emperor chain formation which also was discussed by Torsvik et al. (2017). If this were the case, paleolatitude shifts from ~48 Myr and earlier may be attributed to TPW rather than latitudinal drifts of the plumes. However, changes in inter-hotspot distances between coeval seamounts cannot be explained by TPW and still imply relative drifts between hotspots.

Further analysis and use of our paleolatitude compilation remains beyond the scope of this study. Without any data between 12 Myr to the present, we cannot confidently use paleolatitudes as a constraint for our analysis of recent hotspot drifts. However, our data analysis of these paleolatitudes are still included for completeness and for their usefulness to future work on APM and plume drifts models for earlier time periods.
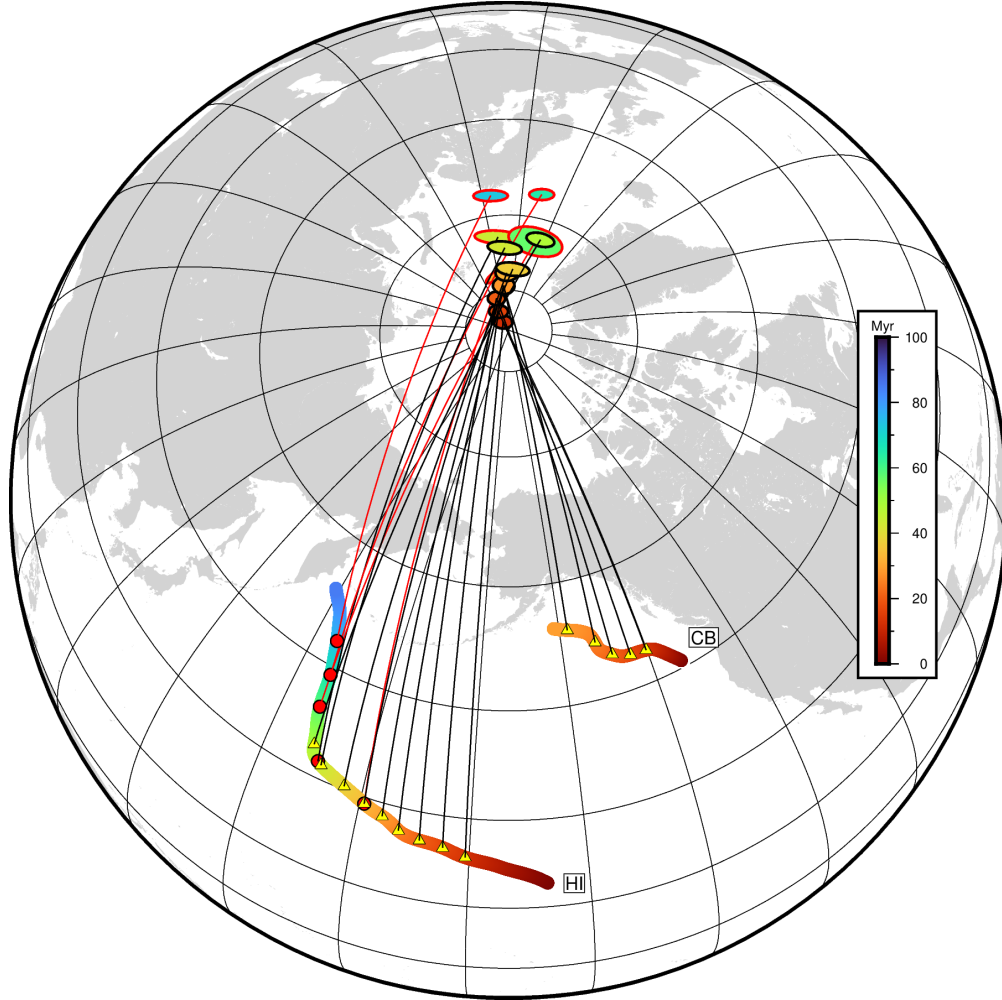
Figure 2.7: Paleo-poles (red outlined ellipses) and paleo-spin axes (black outlined ellipses) with their coeval positions along HI and CB (yellow triangles for the spin-axes and red circles for the paleo-poles). Great circle distances between poles and seamounts are shown by the red lines for the paleo-poles and black lines for the paleo-spin-axes. These distances are the inferred paleo-colatitudes at the given ages and paleolatitudes are trivially computed.

Hawaiian-Emperor Paleolatitudes
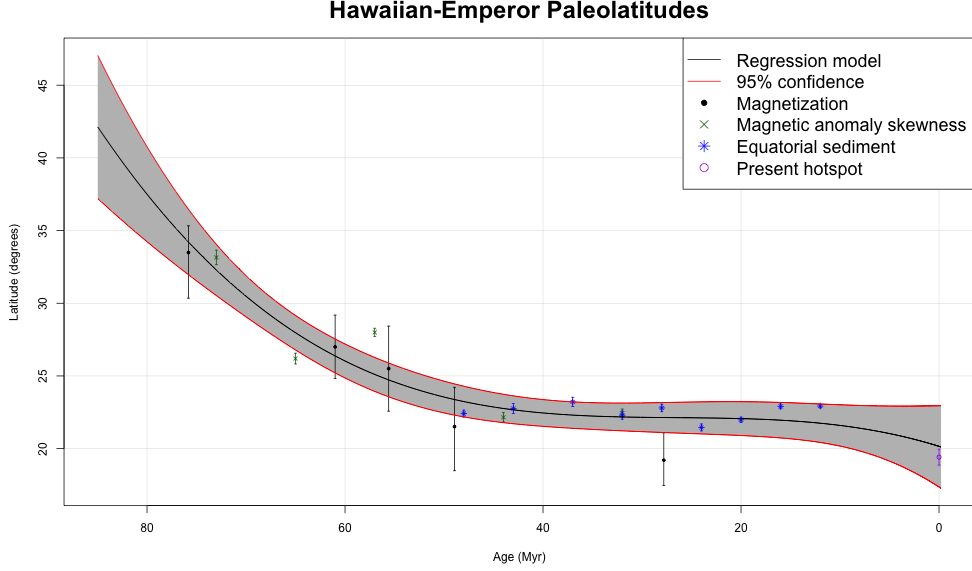
Figure 2.8: Paleolatitudes for the Hawaiian-Emperor chain and the present day hotspot latitude fit by a third order polynomial regression. Present day hotspot latitudes are defined by the zero age on the age progression curves. Similar figures for the remaining chains with paleolatitude data are shown in **Figure A.5**.

2.5 Separations Between Coeval Seamounts

With all eleven seamount chains having a continuous hotspot path with across-track uncertainty and continuous age progression with along-track uncertainty, any chain pair has a continuous range of coeval points. With this information, we now have the ability to calculate the great circle distance between any two coeval points of any two chains. This distance records the frozen-in separation between the two hotspots at the specified time (Wessel and Kroenke 2009). This procedure was repeated for each chain pair combination for the given age range, giving us observed inter-hotspot distances with uncertainties between all 55 combinations provided by the eleven hotspot chains examined in this study. Examples from three chain pairs with the longest age range (HI, LV, and RU) are shown in **Figure 2.9**, with the complete set of 55 provided in **Figure A.4**.

Changes in inter-hotspot distances between coeval points along seamount chains over time infer relative drifts between every pair of hotspots and act as important constraints on the modeling of plume drifts (e.g. Wessel and Kroenke 2009; Wessel 2012; Bono et al. 2019). In this study, these separations and uncertainties were derived from the hotspot trails and age progressions curves presented in **Sections 2.2** and **2.3** respectively. Since every point along each chain is given across-track and along-track uncertainties, total uncertainty in inter-hotspot distances was determined by the methodology of Andrews et al. (2006) for adding unequal elliptical uncertainties. Results from

16

past studies (Wessel 2012) have suggested an inconsistency where the paleolatitude separations between HI and LV surpassed their total inter-hotspot distances. In this study, we found a similar inconsistency, however, it was more subtle and within the margins of error.

The inter-hotspot distances between the three long-lived chains (see **Figure 2.9**) show comparisons with the predictions of Doubrovine et al. (2012), herein called D2012, which predicts plume drifts by modeling flow of the mantle. These predictions show both consistencies and inconsistencies in certain places with the results from our data analysis. The decrease in inter-hotspot distance between HI and LV for $\sim 75 - 45$ Myr observed in our data is consistent with the predictions of D2012 which remain within the margins of error for our data. However, inconsistencies with HI and LV occur during the last ~ 40 Myr, where there is a $2°$ offset between the data and the D2012 predictions. The HI and RU pairs show a similar offset between the data and D2012 predictions during the same time period as HI and LV. The D2012 model also predicts a decrease in inter-hotspot distance between $\sim 80 - 60$ Myr whereas the data suggest a slight increase between HI and RU. There is consistently very little relative drift between LV and RU in both the data and D2012 predictions the last 20 Myr. However, the data available for the two chains in the given time period are scarce and results should be taken with caution. For the $\sim 75 - 45$ Myr time period there is ample data for both the LV and RU chains and the data suggest a prominent decrease in inter-hotspot distance, whereas the D2012 predictions imply a much more gradual decrease for the same time frame. Ideally, derived inter-hotspot separations should constrain models for plume motions (such as D2012), as otherwise such errors will propagate into the plate motion parameters and bias the results.

There is a prominent sharp decrease in inter-hotspot distance between HI and LV, and HI and RU, for the last ~ 5 Myr. This may be an artifact of the high precision of both seamount and age data we have for the youngest portion of HI, whereas for LV and RU data in this region/time period are scarce. It could also be an indication of southward motion of the HI plume during this period. However, more data are available during this time period for most of the shorter-lived chains, and therefore further analysis of those chains may be more suitable when examining relative drifts for the more recent time periods, while chains like LV and RU may be better for the analysis of earlier time periods.

2.6   Hotspot Drift Rates from 6 Ma - Present

There has been much focus on and interest in the inter-hotspot distances between the long-lived chains (e.g. HI, LV, and RU, see **Figure 2.9**) in the Pacific (Wessel and Kroenke 2009; O'Connor et al. 2013; Konrad et al. 2018; Bono et al. 2019). These long-lived chains show variable relative drifts between the hotspots, with periods of very little drift to periods that show more rapid
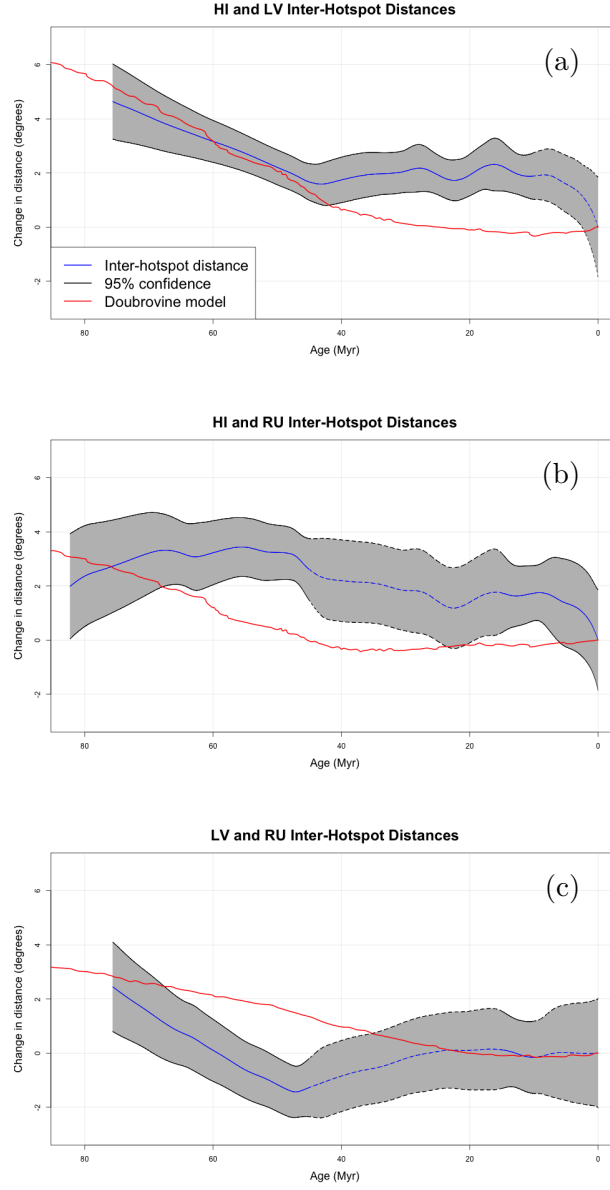
Figure 2.9: Inter-hotspot distances among three chains (HI, LV, and RU). Dashed lines indicate points along one of the chains in the pair with large gaps of little to no data ($\sim 0 - 10$ Myr for LV and $\sim 15 - 45$ Myr for RU). The red line represents predictions of the Doubrovine et al. (2012) model.

18

relative drifts, most notably the decrease in inter-hotspot distance between HI and LV prior to ~ 45 Ma. However, analysis of inter-hotspot distances between pairs of shorter lived chains show a near-linear trend in most cases (e.g. **Figure 2.10** and **Figure A.4**). The linearity of trends allows us to assume a constant relative drift rate between hotspot pairs starting between $\sim$15–5 Ma to the present depending on the longevity of the chain. For this study we have chosen to look at these relative drift rates from the time of 6 Ma to the present. This time frame was chosen because it approximately matches the age of the two shortest-lived chains, MQ and SO, and also because of interest in a proposed change in Pacific plate motion starting at ~ 6 Ma (e.g. Cox and Engebretson 1985; Pollitz 1986; Wessel and Kroenke 2000, 2007; Austermann et al. 2011) .

Using the continuous inter-hotspot distance findings (see **Appendix A.3**), we lack the ability to determine uncertainty and test for significance of the linear fit of these relative drifts. To account for this issue, inter-hotspot distances must be broken into discrete points that represent our age data while also allowing each data point from one chain to have coeval points along the other chain. To most fairly determine a linear fit and its significance for every chain pair's inter-hotspot distance, these distances were sampled at points where radiometric age data were projected onto the inferred hotspot paths (see **Figure 2.5** and **Figure A.1**). However, very rarely do we find coeval points along two chains using these discrete projected data points. To objectively determine coeval points on other chains from the projected data, we use the age progressions found from the least-squares regression fits from **Section 2.3**. Therefore, given chain 1 and chain 2, the data used to determine a linear fit to their inter-hotspot distances are the distances from the projected age data of chain 1 to the coeval point on the continuous age-progressive line of chain 2 and vice versa. An example of this method is shown in **Figure 2.11**. The inferred relative drift rates for each chain pair are summarized in **Table 2.1** with one-sigma uncertainties of these relative drifts summarized in **Table 2.2**.

Not every hotspot chain has adequate age data coverage for the time frame of $6 - 0$ Ma. The Louisville trail contains just one age data point and very little seamount data in the chosen time frame. Rurutu contains only two age data points and both are found at the younger end, at less than 2 Ma. While Caroline also contains just two age data points, the coverage is more spread out, with one sample at the younger end and one at the older end of the $6 - 0$ Ma time frame. Caroline also has a more sufficient coverage of seamount data to constrain trail geometry. The remaining chains (HI, CB, KO, FD, PC, SA, MQ, and SO) have three or more age data points and a clear trail of seamounts in the $6 - 0$ Ma time frame. Therefore, the constant relative drift rates for LV and RU are not included in further analysis of hotspot drifts during this time period.

Hotspot Drifts Relative to Samoa
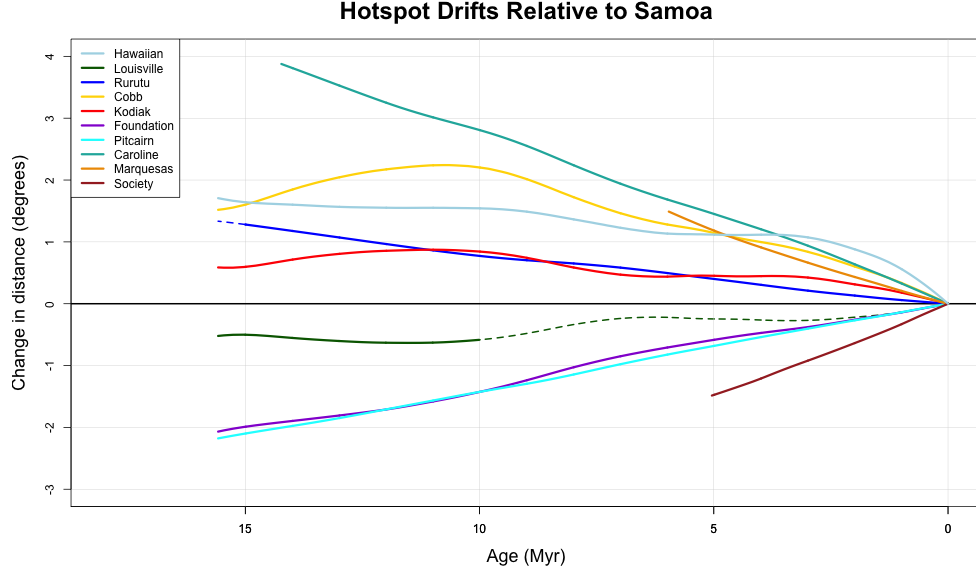
Figure 2.10: Change in inter-hotspot distances between the Samoa seamount chain and all ten other chains from this study, inferring the relative drifts between Samoa and the other hotspots. The present change in inter-hotspot distances is defined to be zero. Coeval positions between chain pairs and their distances are derived from the inferred hotspot trails and age progressions determined in **Section 2.2** and **Section 2.3**. For similar plots of other hotspots see **Appendix A.3**.

HI and MQ Relative Drift Rate
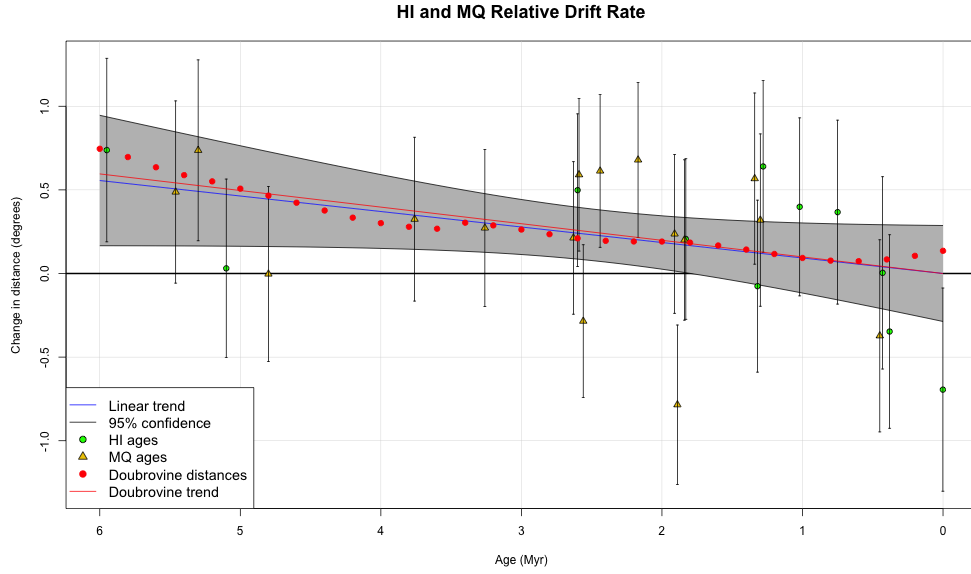
Figure 2.11: A weighted linear least-squares regression fit to the inter-hotspot distance data of the Hawaiian and Marquesas hotspot chains. Weights for the regression were based on the along-track and across-track uncertainties of each chain estimated herein (e.g. **Figure 2.2**) and combined using the methodology of Andrews et al. (2006). The red circles represents prediction of the Doubrovine et al. (2012) model with a linear fit to those predictions (red line).

Relative Drift Rates Between Hotspot Pairs (°/Myr)										
Hotspot	LV	RU	CB	KO	FD	PC	SA	CR	MQ	SO
HI	0.260	0.177	0.126	-0.097	0.076	0.111	0.138	0.068	0.093	0.092
LV		1.195	0.073	0.020	0.194	0.121	-0.087	0.372	0.343	0.251
RU			-0.058	-0.158	0.148	-0.199	-0.034	0.217	0.267	-0.023
CB				-0.023	-0.214	-0.062	0.196	0.342	-0.239	-0.035
KO					-0.264	-0.139	0.073	0.142	-0.304	-0.155
FD						0.071	-0.169	0.433	-0.068	0.148
PC							-0.206	0.147	0.047	0.137
SA								0.365	0.201	-0.309
CR									0.454	0.008
MQ										0.370

Table 2.1: Relative drift rates between all hotspot pairs. See **Figure 2.11** for an example of how these relative drifts were determined. For uncertainties see **Table 2.2**. Two hotspots moving towards each other have a positively defined relative drift rate, therefore a decrease in separation would give a positive relative drift rate.

One-Sigma Uncertainty of Relative Drifts (°/Myr)										
Hotspot	LV	RU	CB	KO	FD	PC	SA	CR	MQ	SO
HI	0.0419	0.066	0.013	0.0216	0.049	0.040	0.011	0.040	0.049	0.048
LV		1.068	0.092	0.084	0.057	0.006	0.017	0.139	0.046	0.047
RU			0.050	0.102	0.079	0.182	0.048	0.300	0.015	0.027
CB				0.132	0.131	0.058	0.008	0.049	0.054	0.036
KO					0.107	0.043	0.006	0.070	0.045	0.023
FD						0.086	0.027	0.134	0.075	0.077
PC							0.020	0.097	0.050	0.067
SA								0.024	0.024	0.035
CR									0.061	0.082
MQ										0.029

Table 2.2: The one-sigma uncertainty for each chain pair's relative drift rate. Uncertainties were determined by the standard deviation of the linear regression fit (see **Figure 2.11**).

CHAPTER 3
MODELING OF HOTSPOT DRIFTS

The rates found in **Section 2.6** (**Table 2.1**) are a set of constant relative drift rates between every hotspot pair (LV and RU are excluded in the analysis) for the given time range $(6 - 0$ Ma$)$. With these inferences from the observations of the linear change in distance between coeval points along the seamount trails, a linear least-squares approach may be used to solve for our parameters of interest, which are the longitudinal and latitudinal drift rates for each hotspot in the system, here represented by v_{ϕ_i}, v_{θ_i} for hotspots $i = 1, n$.
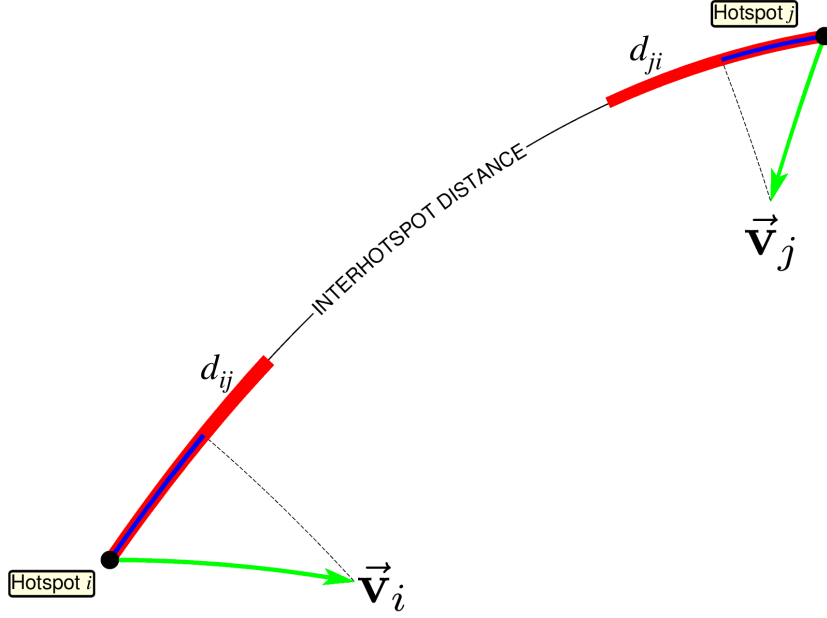
Figure 3.1: Hotspot i and j connected by their great circle. Both hotspots have a true drift described by a vector with a given rate and azimuth (green arrows). The parallel components of the drift rate vectors to the great circle distance (blue lines) show a single hotspot's contribution to that pair's relative drift rate. The sum of the two blue lines gives the total relative drift rate between hotspots i and j (red lines) which are the observations we call d_{ij}.

The sketch from **Figure 3.1** gives a visual representation for our observation (the relative drift rate, d_{ij}) and how it relates to the true drift of the two hotspots. While we cannot observe the hotspot drift vectors directly, we can observe changes in inter-hotspot distances from seamount

chains, allowing us to infer a *relative* drift rate between the pair. Each hotspot in the pair contributes its parallel component along the great circle connecting the hotspots. However, we can only observe the sum of these parallel components, therefore making us unable to determine how much each hotspot contributes to the observed rate by looking at just the two hotspots alone. Adding more hotspots and establishing prime constraints to the system, therefore, allows for a linear least-squares solution that may resolve the drift vectors for each hotspot.

We must therefore describe the relative drift rates, d_{ij}, between hotspot i and j in terms of our parameters, v_{ϕ_i} and v_{θ_i}. We also must constrain the net translation and rotation of the hotspot group, since any such absolute motions will not be reflected in our relative rate observations. Since our system of hotspots used for this study spans a wide area of the Pacific plate, the equations that describe the least-squares misfit and the constraints must work on the surface of a sphere. Here we present a new method for inverting such data.

3.1 Least-Squares Equation

We start with an n hotspot system on the surface of a sphere, with surface coordinates defined by longitude, ϕ, and latitude, θ, with ϕ increasing eastward and θ increasing northward from $-90°$ at the south pole to $90°$ at the north pole. The transformation between spherical and Cartesian components is given by the standard relationship

$$\begin{bmatrix} v_x \\ v_y \\ v_z \end{bmatrix} = \begin{bmatrix} -\sin\phi & -\sin\theta\cos\phi & \cos\theta\cos\phi \\ \cos\phi & -\sin\theta\sin\phi & \cos\theta\sin\phi \\ 0 & \cos\theta & \sin\theta \end{bmatrix} \begin{bmatrix} v_\phi \\ v_\theta \\ v_r \end{bmatrix} = \boldsymbol{C} \cdot \begin{bmatrix} v_\phi \\ v_\theta \\ v_r \end{bmatrix}. \tag{3.1}$$

The third column in $\boldsymbol{C}$ describes the $\hat{\boldsymbol{r}}_i$ position of hotspot i on the surface of the unit sphere:

$$\hat{\boldsymbol{r}}_i = \cos\theta_i \cos\phi_i \hat{\boldsymbol{x}} + \cos\theta_i \sin\phi_i \hat{\boldsymbol{y}} + \sin\theta_i \hat{\boldsymbol{z}}. \tag{3.2}$$

Our model parameters are the components of a velocity vector, $\boldsymbol{v}_i$, that is required to be tangent to the surface of the unit sphere, i.e.,

$$\mathbf{v}_i = v_{\phi_i} \hat{\boldsymbol{\phi}}_i + v_{\theta_i} \hat{\boldsymbol{\theta}}_i. \tag{3.3}$$

The rotation vector associated with $\boldsymbol{v}_i$ is simply

$$\boldsymbol{\omega}_i = \hat{\boldsymbol{r}}_i \times \mathbf{v}_i, \tag{3.4}$$

where $\times$ denotes the usual cross product. Combining Equations 3.3 and 3.4 and using the right-hand rule for cross-products we can write $\boldsymbol{\omega}_i$ in terms of our parameters v_{ϕ_i}, v_{θ_i}:

$$\boldsymbol{\omega}_i = \hat{\boldsymbol{r}}_i \times (v_{\phi_i}\hat{\boldsymbol{\phi}}_i + v_{\theta_i}\hat{\boldsymbol{\theta}}_i) = v_{\phi_i}\hat{\boldsymbol{r}}_i \times \hat{\boldsymbol{\phi}}_i + v_{\theta_i}\hat{\boldsymbol{r}}_i \times \hat{\boldsymbol{\theta}}_i = -v_{\theta_i}\hat{\boldsymbol{\phi}}_i + v_{\phi_i}\hat{\boldsymbol{\theta}}_i. \tag{3.5}$$

The rotation and velocity vectors that describe a hotspot's motion on the surface of a sphere is most clearly expressed in a local spherical $(\hat{\boldsymbol{\phi}}, \hat{\boldsymbol{\theta}}, \hat{\boldsymbol{r}})$ coordinate system. However, converting these vectors to a global Cartesian $(\hat{\boldsymbol{x}}, \hat{\boldsymbol{y}}, \hat{\boldsymbol{z}})$ coordinate system is later needed when forming vector operations with other vectors in the same global Cartesian coordinate system. To simplify the derivation, matrices are constructed to perform these coordinate system transformations.

Since hotspot motions are tangent to the Earth's surface, $v_r \equiv 0$, therefore the third column in $\boldsymbol{C}$ can be ignored. Furthermore, the conversion from velocity to rotation vector, i.e., Equation 3.5 can be written, $\boldsymbol{\omega} = \boldsymbol{J} \cdot \boldsymbol{v}$, where

$$\mathbf{J} = \begin{bmatrix} 0 & -1 \\ 1 & 0 \end{bmatrix}. \tag{3.6}$$

The transformation matrix for surface vectors thus becomes

$$\mathbf{T} = \mathbf{C} \cdot \mathbf{J} = \begin{bmatrix} -\sin\theta\cos\phi & \sin\phi \\ -\sin\theta\sin\phi & -\cos\phi \\ \cos\theta & 0 \end{bmatrix}. \tag{3.7}$$

We find the polar axis of the great circle between hotspot i and j via

$$\hat{\boldsymbol{u}}_{ij} = \frac{\hat{\boldsymbol{r}}_i \times \hat{\boldsymbol{r}}_j}{|\hat{\boldsymbol{r}}_i \times \hat{\boldsymbol{r}}_j|}. \tag{3.8}$$

The misfit, E, that we seek to minimize involves the squared difference between the predicted and observed relative drift rates and takes the form of a weighted sum for each hotspot pair:

$$E = \sum_{i=1}^{n} \sum_{j=1}^{n} \left[\frac{d_{ij} - d'_{ij}}{s_{ij}} \right]^2 \quad i \neq j, \tag{3.9}$$

where n is the number of hotspots, d_{ij} is the observed (**Table 2.1**) and d'_{ij} is the predicted relative drift rate between hotspot i and j, and s_{ij} is the one-sigma uncertainty in the observed relative drift rate (**Table 2.2**). Predicted relative drift rates are given by the projected contributions from the two hotspots' drift onto the great circle:

$$d'_{ij} = \hat{\boldsymbol{u}}_{ij} \cdot (\boldsymbol{\omega}_i - \boldsymbol{\omega}_j) = \hat{\boldsymbol{u}}_{ij} \cdot (\boldsymbol{T}_i\boldsymbol{v}_i - \boldsymbol{T}_j\boldsymbol{v}_j). \tag{3.10}$$

Equation (3.10) thus relates our observations to the unknown parameters.

3.2 No-Net-Translation Equation

Any net motion in the longitudinal and latitudinal directions can be thought of as a rotation around a fixed distance pole shifting all the hotspot drifts by their longitudinal and latitudinal components simultaneously. However, such related motions would cancel in our estimates for d_{ij}. Hence, in order to constrain this net motion we must sum all the hotspot's translational drifts, take the average and set it equal to zero. Therefore, the no-net-translation constraint ensures the hotspot group's average drift rate is zero and is given by,

$$\mathbf{0} = \frac{1}{n}\sum_{i=1}^{n}\boldsymbol{\omega}_i = \frac{1}{n}\sum_{i=1}^{n}\boldsymbol{T}_i \cdot \boldsymbol{v}_i. \tag{3.11}$$

3.3 No-Net-Rotation Equation

Similar to the no-net-translation constraint, we must also constrain any net rotation about the centroid of all the hotspots. To get hotspot rotation rates about the centroid, we must calculate the centroid on the surface of the unit sphere, $\hat{\mathbf{c}}$, the polar angle of hotspot i to the centroid axis, ψ_i, and the tangent vector to the small circle through $\hat{\boldsymbol{r}}_i$, called $\hat{\boldsymbol{t}}_i$:

$$\hat{\mathbf{c}} = \frac{\sum_{i=1}^{n}\hat{\mathbf{r}}_i}{\left|\sum_{i=1}^{n}\hat{\mathbf{r}}_i\right|}, \tag{3.12}$$

$$\psi_i = \cos^{-1}(\hat{\mathbf{c}} \cdot \hat{\mathbf{r}}_i), \tag{3.13}$$

$$\hat{\mathbf{t}}_i = \frac{\hat{\mathbf{c}} \times \hat{\mathbf{r}}_i}{|\hat{\mathbf{c}} \times \hat{\mathbf{r}}_i|}. \tag{3.14}$$

The rotation rate of hotspot i about the centroid is

$$\omega_i' = \frac{\mathbf{v}_i \cdot \hat{\mathbf{t}}_i}{\sin\psi_i}. \tag{3.15}$$

The no-net-rotation equation is therefore

$$\frac{1}{n}\sum_{i=1}^{n}\omega_i' = \frac{1}{n}\sum_{i=1}^{n}\frac{\hat{\mathbf{t}}_i}{\sin\psi_i} \cdot \mathbf{v}_i = 0. \tag{3.16}$$

Coupled with **Equation 3.11** we ensure that our solutions will be free of any group translation and rotation. Using the methods of Menke (2018) for constrained least-squares problems, our least-squares equations, constraint equations, parameters, and observations are organized into a set of

matrix equations from which an optimal solution is found.

3.4   Testing on Synthetic Data

Before obtaining results from this modeling scheme using our relative drift rate observations, it was first attempted on a synthetic data set. The synthetic data contained a chosen number of hotspots, each with a known absolute drift rate magnitude and azimuth. The relative rates from this data, which are our synthetic "observations", were calculated by

$$d_{ij_{synthetic}} = r_i \cos(\alpha_{ij} - a_i) + r_j \cos(\alpha_{ji} - a_j), \tag{3.17}$$

where r_i and a_i are the absolute drift rate and azimuth of hotspot i respectively, and α_{ij} is the azimuth from hotspot i to hotspot j along the great circle connecting them. With these calculations we have a set of synthetic observations that are equivalent to the observations we have with our relative hotspot drift rate data. From here we can set up a system of hotspots with prescribed absolute drifts, attain the relative rates, and use the relative rates in our model to test if the solutions match the prescribed drifts. However, since our method constrains for no-net-translation and no-net-rotation, we set up the synthetic case to have neither of these net motions so we can directly compare prescribed and resolved drifts (see **Figure 3.2**). Our synthetic case showed us that the method was stable and could reproduce the prescribed data exactly. We also used a Monte Carlo simulation to check that our formal error estimates were consistent with results from the simulation. Our findings showed consistency between errors for the two methods, giving us more confidence in the formal error calculations on the real data.

3.5   Results

The predicted hotspot drifts found using the methods explained in this chapter are summarized in **Figure 3.3** and **Table 3.1**. This figure shows the raw solutions satisfying the no-net-translation and no-net-rotation criteria. These raw solutions do not necessarily represent the true absolute hotspot motions because they do not capture any mean group rate of all the hotspots. However, if there is very little or no mean group rate then these results would be reflections of absolute hotspot motions from 6 Ma to the present. In order to compare how removing specific hotspots from the system affects the drift solutions for the remaining hotspots, we attain the solutions for each scenario of removing one hotspot. Each panel displays the solution drift vectors of that specific hotspot for all the eight possible scenarios that exclude one of the other hotspots. For comparison, **Figure 3.4** shows the solutions relative to a fixed Hawaiian hotspot. This solution is found by describing the HI drift solution as a rotation via Equation (3.16) and subtracting the rotation from the solutions of the other hotspots. This creates a constant and well-defined reference frame for the

Synthetic Data Solution
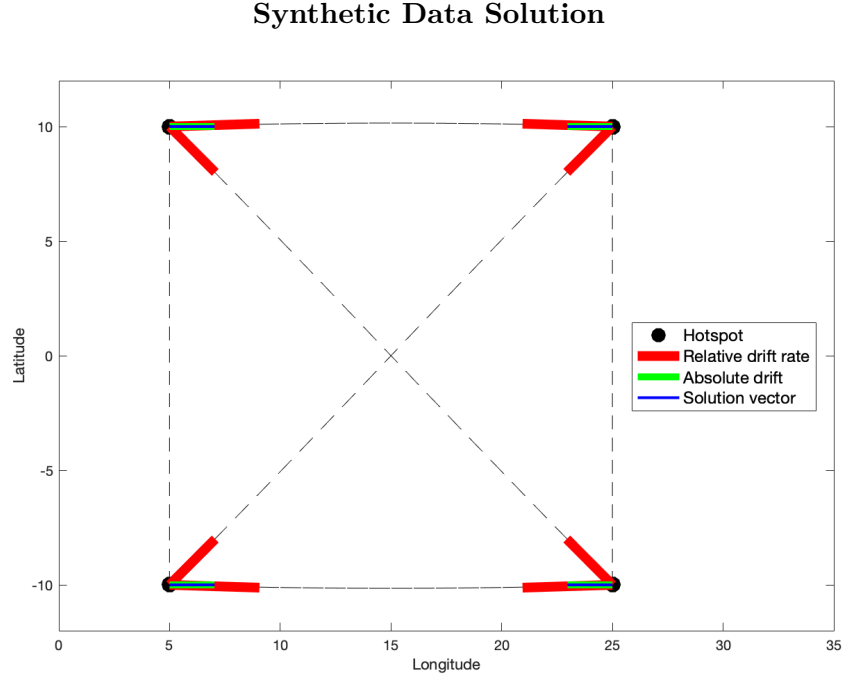
Figure 3.2: A synthetic data set with four hotspots given a geometry and prescribed absolute drifts that allows for no-net-translation and no-net-rotation within the system. The dashed lines represent the great circles connecting all the hotspot pairs. For this no-net-motion system, the solutions perfectly match the known drifts of the hotspots, affirming our model works to solve for hotspot drifts in a no-net-rotation reference frame.

hotspot drifts that allows for a better comparison of solutions when removing or adding hotspots to the system. The Hawaiian hotspot was chosen as the reference frame for two reasons: a) The raw solutions consistently found HI to have only a small amount of motion compared to the other hotspots, and b) the absolute drift of HI from the prediction of the D2012 model is also insignificantly small compared to the other hotspots for this time frame. In the next chapter we will discuss our results and compare to them to conclusions from other studies for determining plume drifts.

Hotspot	Rate (°/Myr)	Azimuth (°)
HI	0.061	129°
CB	0.266	-67°
KO	0.159	-30°
FD	0.403	-155°
PC	0.106	48°
SA	0.189	-23°
CR	0.206	94°
MQ	0.173	-103°
SO	0.287	100°

Table 3.1: The rates and azimuths of the hotspot drift solutions when all 9 hotspots are included in the inversion. This solution explains 95.86% of the variance.
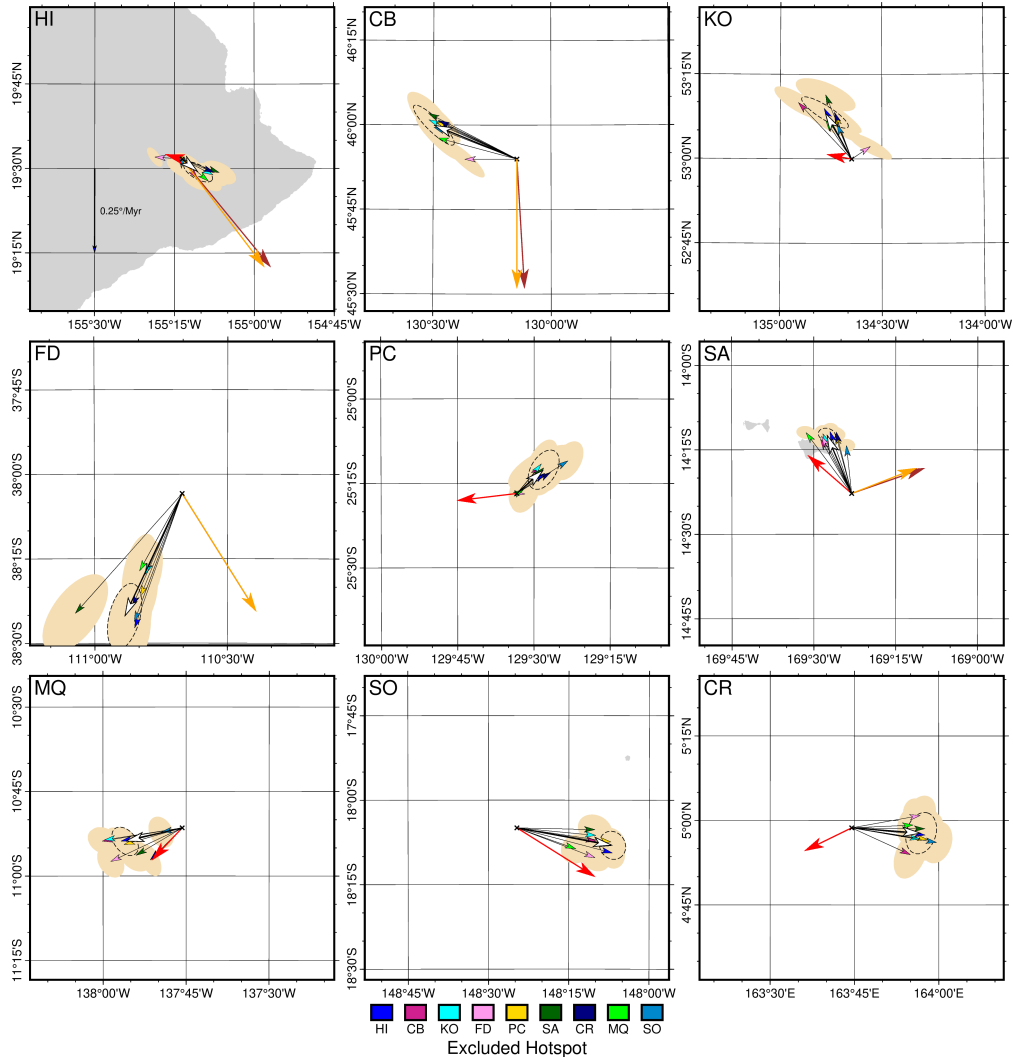
Figure 3.3: The solution drift vectors for all 9 hotspots modeled (white arrows), the 95% confidence ellipses for these solutions (dashed ellipses), the solutions with the exclusion of one hotspot from the system (colored arrows), the 95% confidence ellipses for these nine solutions (tan ellipses), the absolute hotspot drift predictions from Doubrovine et al. (2012) (red arrows), the predictions from the Tetley et al. (2019) OptAPM1-M16 (brown arrows) and OptAPM1-s13 (orange arrows) models. FD has identical drifts for both Tetley et al. (2019) models, so only one appears. Each hotspot is plotted in a separate panel with the same dimensions (100 km x 100 km) with the hotspot location directly in the middle (black x's). A vector scale is displayed in the upper-left-hand (Hawaiian hotspot) panel and applies to every vector plotted in the figure.
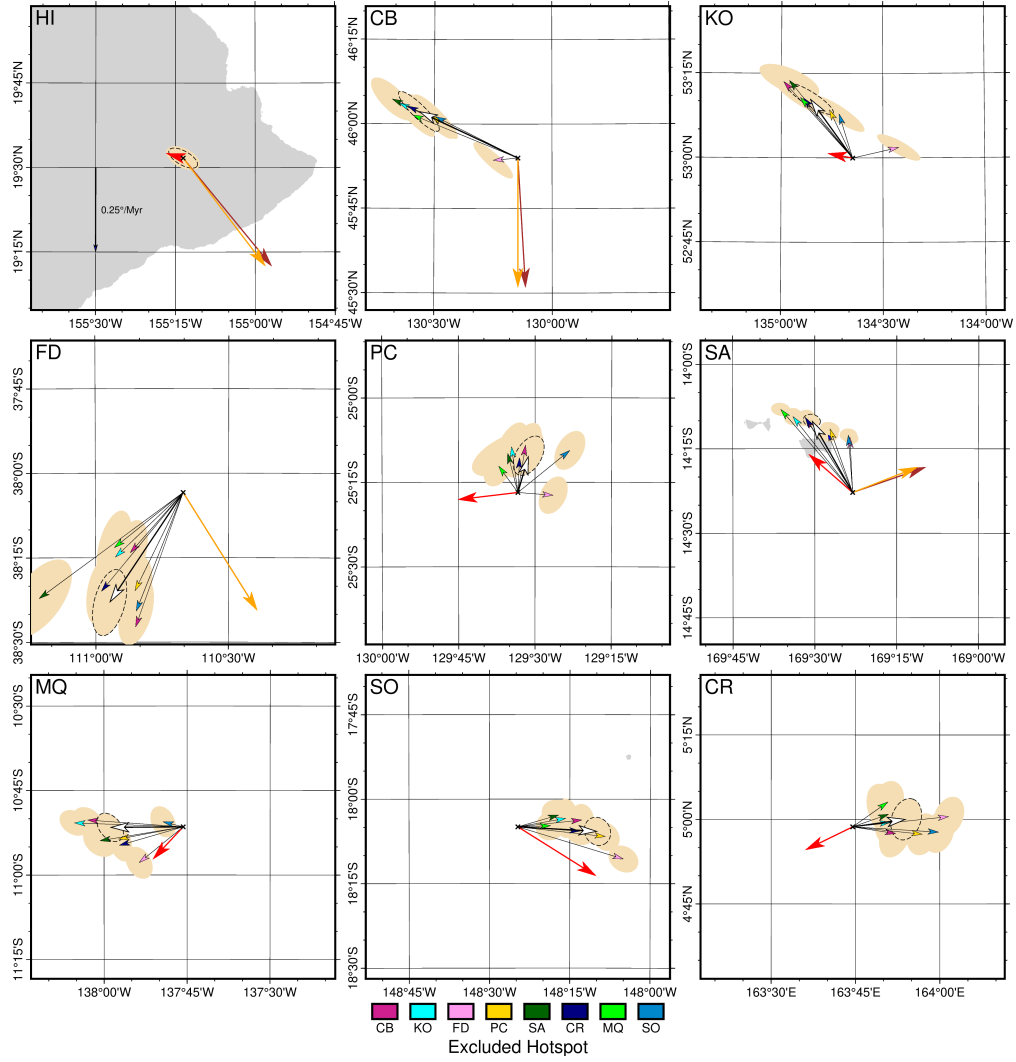
Figure 3.4: The solution vectors in the reference frame of the Hawaiian hotspot. See **Figure 3.3** caption for symbol explanations.

CHAPTER 4
DISCUSSION

The work from **Chapter 2** has produced a carefully processed set of spatial time-series capturing geometric age and paleolatitude progressions with uncertainties for eleven Pacific seamount chains. These data can be used for further analysis and serve as prime constraints for future plate and plume motion modeling. In this paper, we used this data to analyze inter-hotspot distances between the long-lived seamount chains (see **Section 2.5**). As a novel use for this data, a modeling scheme described in **Chapter 3** was used to solve for recent hotspot motions. Results from this method of solving for plume drifts are discussed through the remainder of this chapter. We compare our results to hotspot drifts predictions from D2012, and Tetley et al. (2019), herein called T2019.

With the results from this study, the D2012 predictions, and the T2019 predictions, we have a comparison of three different assessments of Pacific hotspot motions for the past 6 Myr. (1) The inversion of observed relative drift rates (this study), (2) predictions from APM modeling that include how plumes are effected by the mantle wind (D2012), and (3) a modeling of Pacific APM in which plume drifts are obtained from the misfit between the predicted seamount trails from a fixed hotspot model and the observed seamount trails (T2019). However, of the 9 hotspots examined in our modeling of plume drifts, the D2012 and T2019 predictions only cover some of them. Specifically, the D2012 model does not include predictions for CB and FD, while the T2019 model does not include predictions for KO, PC, MQ, SO, and CR.

The solution vectors plotted with their uncertainty ellipses in **Figures 3.3** and **3.4** suggest significant absolute drifts of the hotspots at the 95% confidence level, with the exception of HI. The 95% confidence ellipse (for the inversion including all hotspots) for HI is within a region that would suggest no drift. This lack of significant drift for HI is consistent with the predictions from D2012 which also suggest no significant absolute drift for HI for the last 6 Ma.

Our results for Caroline show a prominent eastward drift of the hotspot. However, this result for Caroline should be considered with caution. The Caroline seamount chain has only three age data points throughout, with two in the $6 - 0$ Ma timeframe. This makes the chain age progression predictions less reliable and therefore decreases our confidence that these changes in distance between coeval seamounts from Caroline to the other chains are the result of relative hotspot drift rather than inaccuracies in our age progression curve. However, excluding Caroline from the hotspot system did not have a significant effect on the solutions for the other hotspots and therefore it is still included in the overall solution.

The D2012 model predictions give absolute drift rates that are consistent with some of the hotspot drift solutions from our study, which include HI, SA, MQ, and SO, while the hotspots KO, PC, and CR show conflicting results. The predictions from the T2019 model show conflicting results from all four hotspots we can make comparisons to (HI, CB, FD, and SA). Furthermore, for cases where we have both D2012 and T2019 predictions (HI and SA), the predictions from the two models have conflicting results. The predictions from the T2019 model may suggest there is a large mean group signal we are missing from our solutions, while the D2012 predictions may suggest there has been very little recent drift of the Hawaiian hotspot, making the mean group rate of the hotspots small or nonexistent.

Of all the hotspots we have D2012 model predictions for, the three where our solutions contradict the predictions from D2012 (KO, PC, and CR) are also the hotspots with corresponding seamount trails where we have the least amount of age data (see **Figure 1.1** and **Figure A.1**). This raises the question of whether the relative drifts we observe from seamount chains with sparser data are the results of hotspot drifts or artifacts of predicted seamount chain age progressions that do not correctly follow the true paths of the hotspot chains. Better data may be required to explore these discrepancies further.

The motion of the Hawaiian hotspot from $6 - 0$ Ma has important implications for recent absolute plate motions. A recent bend in the Hawaiian chain suggests either a recent southward shift in the Hawaiian hotspot drift or a more northerly shift in Pacific plate motion (Cox and Engebretson 1985; Pollitz 1986; Wessel and Kroenke 2000, 2007, 2008; Austermann et al. 2011). Our results for the Hawaiian hotspot and the consistency with the D2012 model predictions that show very little drift of the hotspot would suggest this change in seamount geometry around 6 Ma is the result of plate motion change. On the other hand, T2019 predictions explain this change in the geometry by a change in plume drift that is moving rapidly to the southeast. Yet, we note this implied motion is simply resolved as a residual misfit between their predicted trail and observed trail.

While paleolatitude data suggest a southward drift of the Hawaiian hotspot sometime between 12 Ma to the present (**Figure 2.8**), these inferences should be taken with caution. The youngest paleolatitude data we have is 12 Ma which comes from shifts in equatorial sediments giving inferred paleo-spin-axes (Woodworth and Gordon 2018; Parés and Moore 2005). This gap in data makes it difficult to determine when this potential southward drift may have occurred by looking at paleolatitudes alone. However, TPW (Goldreich and Toomre 1969; Tsai and Stevenson 2007) may also explain the apparent southward change in paleolatitude without the need for a southward drift of the Hawaiian hotspot (Woodworth and Gordon 2018). We note hotspots LV and RU show similar

paleolatitude trends (see **Appendix A.4**), which could support either a southward mean group rate of the hotspots or recent TPW. Unfortunately, both chains have very little age and seamount data for the more recent time periods, with no well-determined hotspot location. This makes it difficult to determine uniquely if there is a significant southward change in paleolatitude since the hotspot locations are so uncertain. Consequently, it also makes our $6-0$ Ma relative drift rate predictions for the two hotspots too unreliable to include in our system that solves for hotspot drifts (**Chapter 3**).

The addition of paleolatitude data from the timeframe $6-0$ Ma would allow us to use paleolatitude as a constraint in our least-squares solution. Constraining the paleolatitude of just two hotspots would fix the group rotation of the hotspots and allow for the system to be solved without a no-net-rotation constraint. However, the paleolatitudes would place no constraints on the longitudinal translation, and therefore the no-net-translation constraint would apply but need to be modified to a no-net-longitudinal-translation constraint. However, the analysis of land based paleolatitude measurements from Pacific island chains is beyond the scope of this work, and therefore these improvements to the model constraints cannot be made at this time for the $6-0$ Ma time frame. Possibly, geodynamic arguments may be used to explore such constraints (e.g. Conrad et al. 2013). However, more work needs to be done to explore these studies on geodymanic models and examine them as suitable constraints to plume drifts.

To our knowledge, the methodology developed in **Chapter 3** is novel and represents the first time inter-hotspot distance variations have been used to directly determine plume drifts. We are hopeful this new method can help shed light on the motion of plumes and thus help improve future APM models. Our findings could also be improved if more data become available, for both seamount age and paleolatitude. This method for finding plume drifts may also be applied to other time periods where there appear to be a constant change in inter-hotspot distance between the seamount chains. Our data set also has future utility beyond our simple analysis of recent plume drifts, which could include the holy grail of developing more robust APM models that aim to solve for plate motions and plume drifts simultaneously over longer time periods.

APPENDIX A

A.1 Square-Root of Age Curve for Determining Filter Widths

Our median filter with varying radii used to obtain the residual bathymetry from **Section 2.1** was assigned a radius based on the age of the seafloor when seamount loading occurred (Δt). A linear function of square root of age verses filter width was constructed based on known ages and filter widths that worked for specific regions. Based on visual inspection of cross sections along the youngest portion of the Hawaiian chain, a filter width of 420 km was found to have properly removed the flexure of the ocean floor due to lithosphere deformation. In the older Emperor region, a similar visual inspection found 330 km to be a reasonable filter width. The crustal age at seamount loading for the young Hawaiian chain is approximately 90 Myr, while we estimated an average loading age for the Emperor chain to be about 48 Myr. This gave us our two points at $(\sqrt{48}, 330)$ and $(\sqrt{90}, 420)$ which defined the linear function used to determine filter width values along a chain:

$$fw = \frac{420 - 330}{\sqrt{90} - \sqrt{48}}\sqrt{\Delta t} + 86 \tag{A.1}$$

A.2 Medial Trail Lines and Age Curves

A large portion of our data analysis of seamount chains involved determining the medial trail lines of the seamount chains and fitting a continuous age progression through them. **Sections 2.1, 2.2, and 2.3** described and gave examples of the processes for determining these age progressive hotspot trails, and here some of the steps and result for the remaining chains are shown.
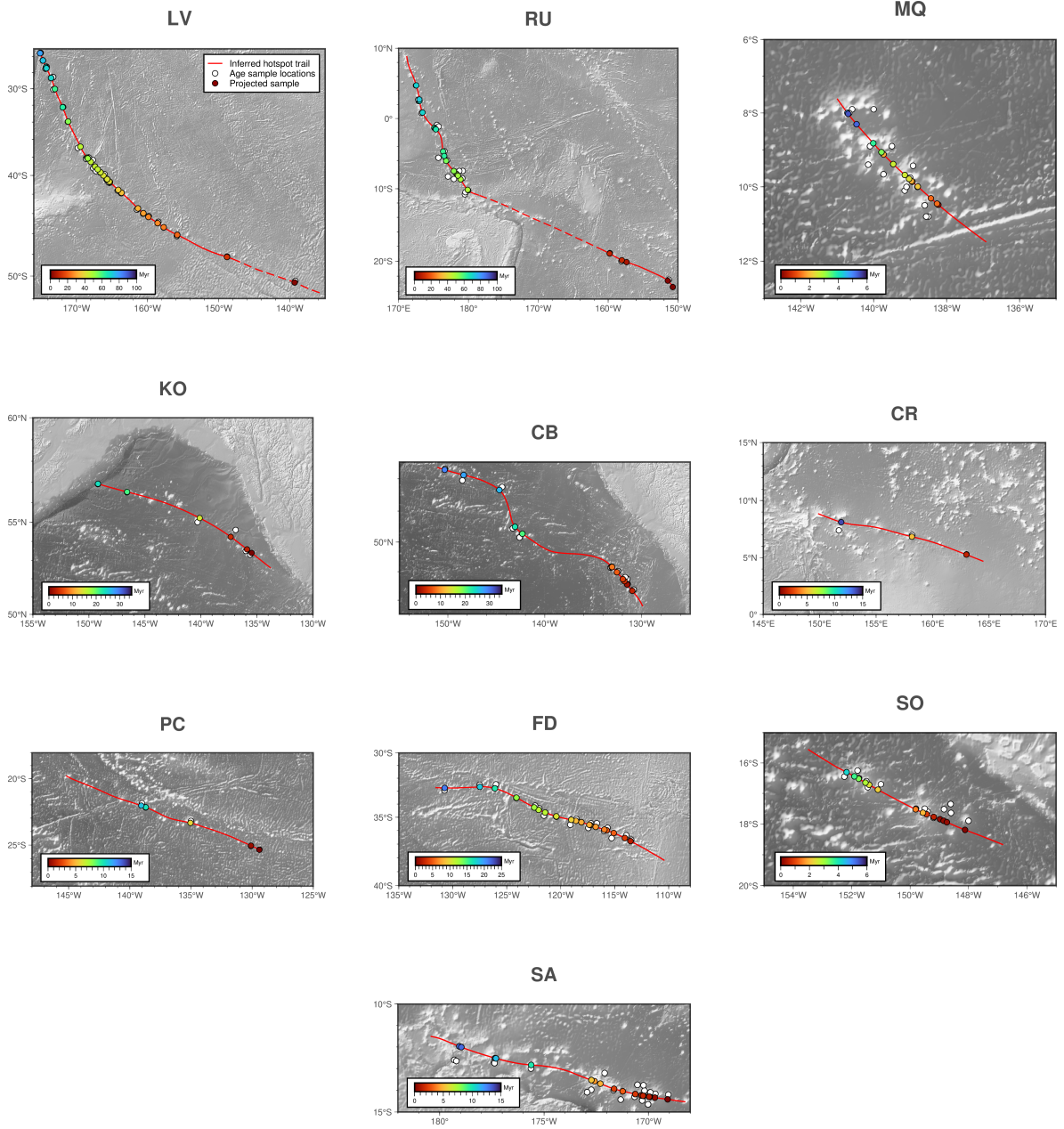
Figure A.1: Medial trail lines (red lines) and radiometric age data locations (white circles) with their projected positions on the medial line (colored circles) for ten of the chains. Dashed lines represent portions of the chain with little to no seamount data. The figure for HI is in the main paper as **Figure 2.5**.
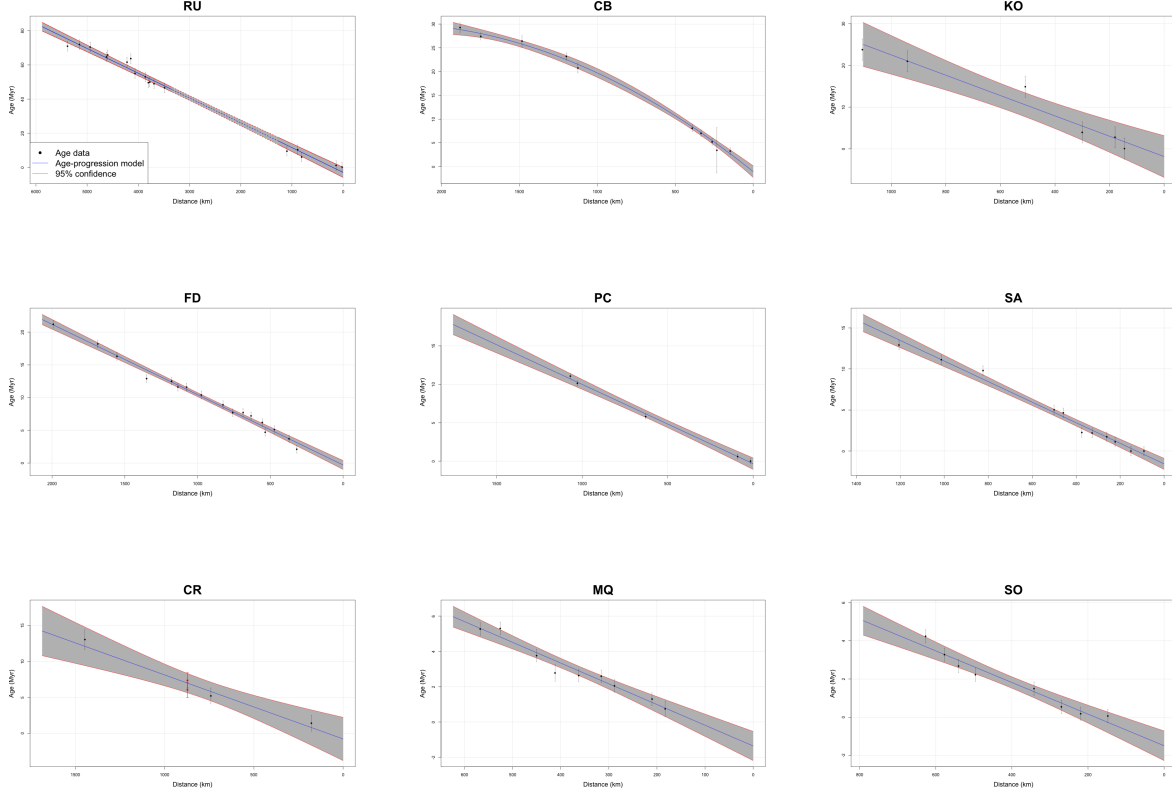
Figure A.2: Binned radiometric age data for nine of the seamount chains with a weighted polynomial regression fit to the data. The models' parameter order is determined by an F-test, where CB is fit with a second-order polynomial and the remaining chains displayed here are fit with a first-order polynomial. Dashed lines represent gaps in the chain where there is little to no seamount data. CR has two added points (red circles) that do not change the trend but help stabilize the uncertainty. Results for HI and LV are displayed in the main paper (see **Figure 2.6**).

Two data points were added to the Caroline age regression that do not change the trend but do change the confidence bands. With only three data points, the small degree of freedom gives unreasonably large confidence bands for the CR regression. Since we understand the dynamics of the system we are fitting a curve to (age progression of seamounts along a chain), and we see a reasonable trend with the three data points, we felt overriding the objectively found uncertainties in the CR age curve was necessary to more accurately reflect the scatter in the data.
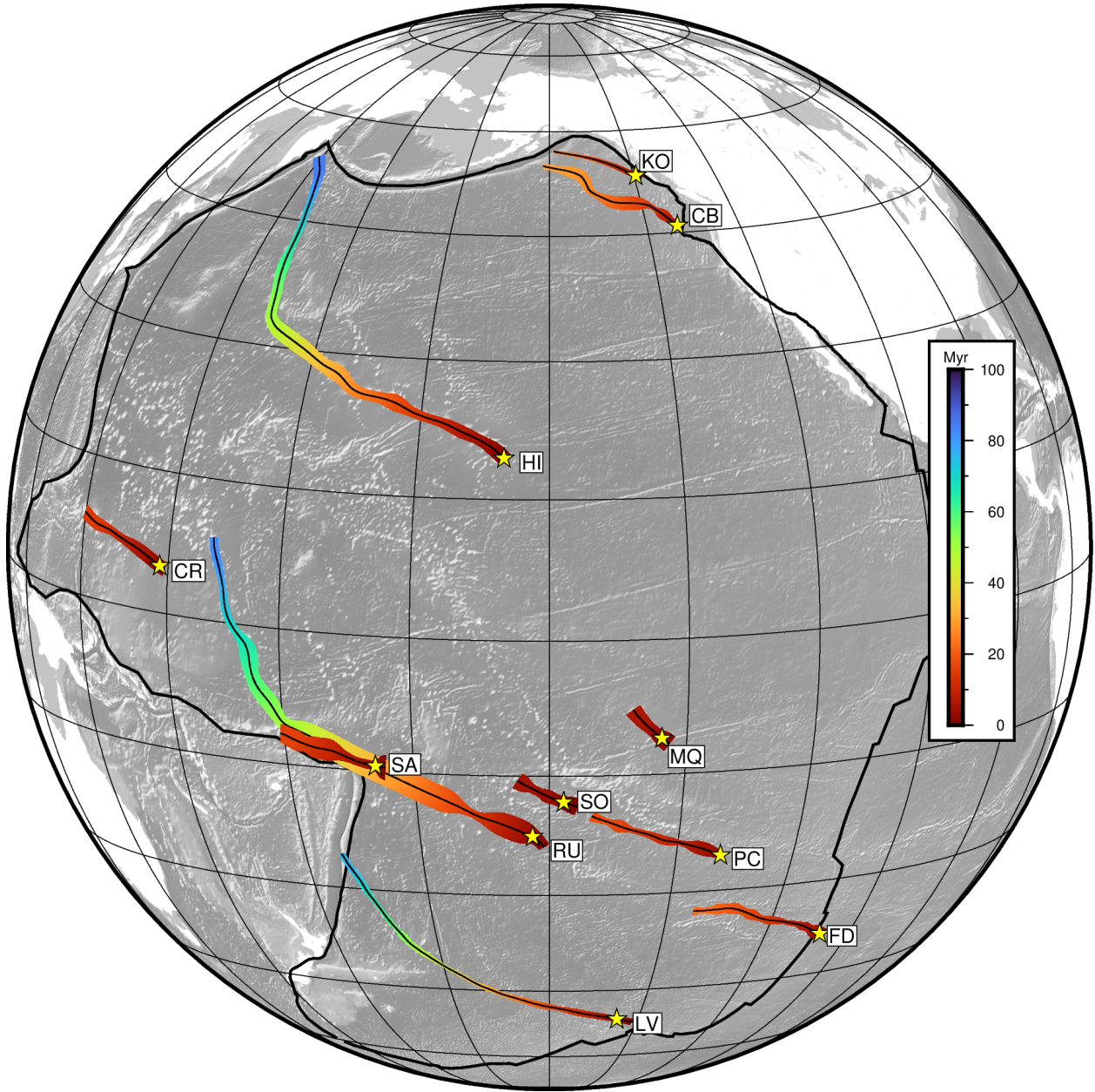
Figure A.3: Summary of all eleven seamount chains' medial trail line (black lines), showing the medial lines' variable across-track uncertainty (colored paths) with their color representing the continuous age progression of the chain. A grey-scale bathymetry grid of the Pacific region is displayed with the Pacific plate boundaries (thick black line). The present hotspot locations (yellow stars) are determined by the zero age of the regression curve, which in some cases is noticeably off from what was defined as zero distance on the medial trail lines (i.e. LV, RU SA, and SO).

A.3 Inter-Hotspot Distances

Based on the age progression curves and medial trail lines from **Sections 2.2** and **2.3** we can determine inter-hotspot distances for every chain pair. Inter-hotspot distances between the three long-lived chains are shown in **Figure 2.9** with a shorter-lived chain shown in **Figure 2.10**. To include inter-hotspot distance results for all eleven chains (55 chain pairs), we include **Figure A.4**.
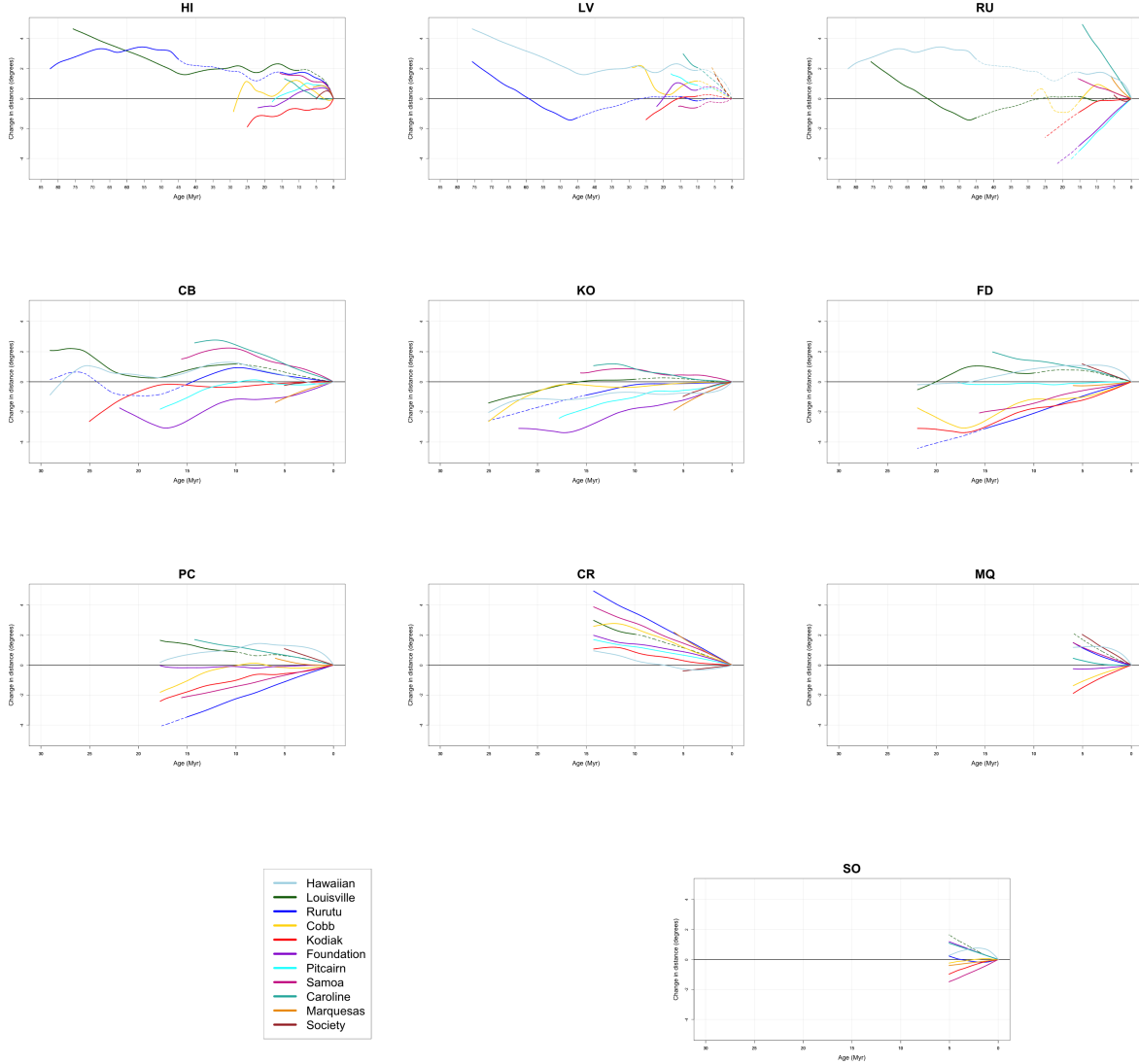
Figure A.4: Inter-hotspot distance results for the other ten chains. Each panel represents a different chain with all the chains' inter-hotspot distances plotted together. The top three panels have a larger range on the x-axis ($85 - 0$ Myr) to accommodate for the longer-lived chains (HI, LV, and RU). The remaining chains all have the same x-axis scale ($30 - 0$ Myr). Dashed lines represent portions where one of the chains in the pair has regions with very little to no seamount data.

A.4 Paleolatitudes

The methods for attaining our paleolatitude curves and an explanation of the different types of paleolatitude data are described in **Section 2.4**, with results for HI displayed in **Figure 2.8**. The remaining chains we have sufficient paleolatitude data to fit a regression curve to (LV, RU, CB, KO, and FD) have their data and curves shown in **Figure A.5**.
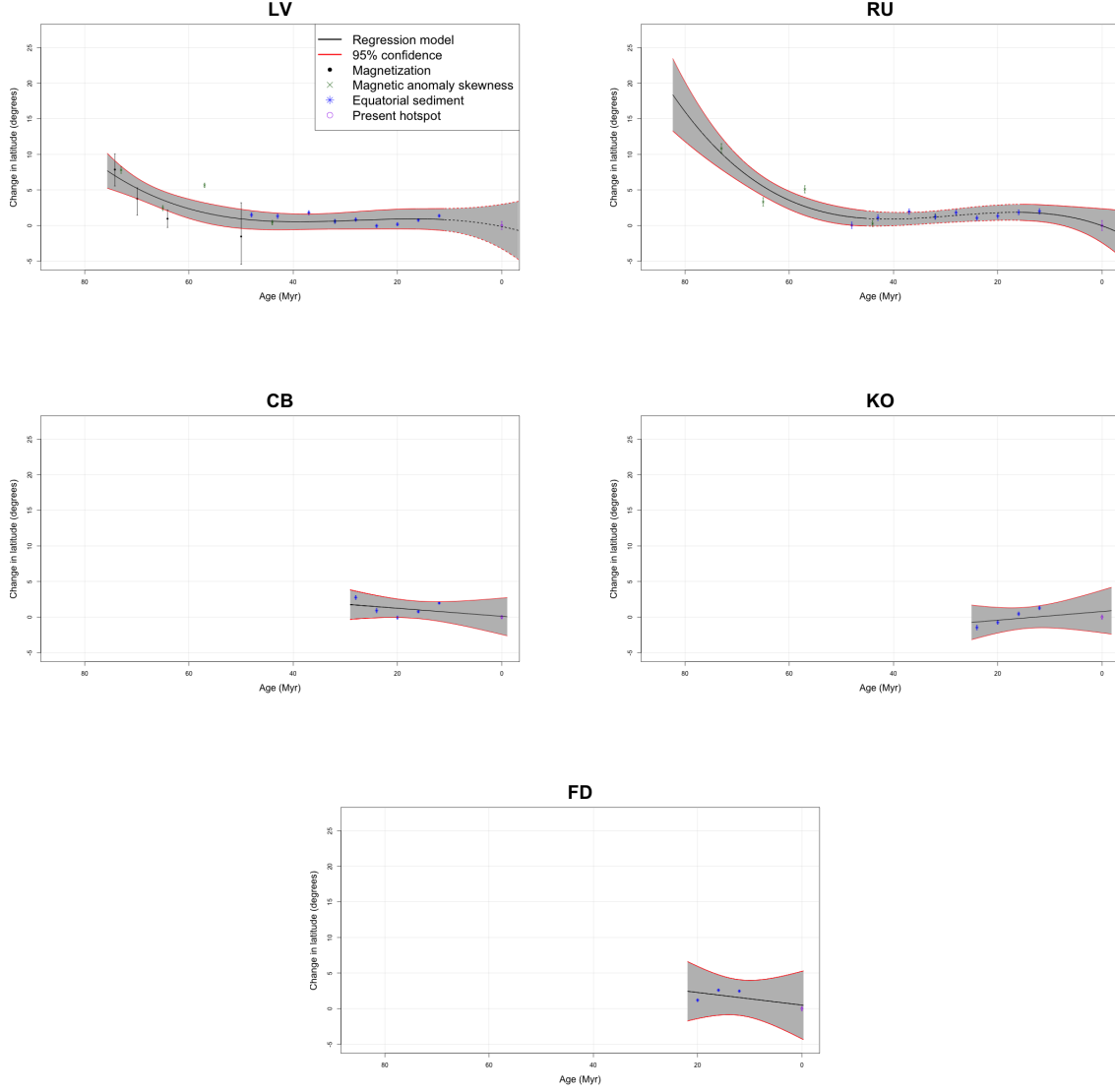
Figure A.5: Paleolatitudes for the LV, RU, CB, KO, and FD chains and the present day hotspot latitude fit by a polynomial regression. LV and RU are fit by a third-order polynomial, while the remaining chains (CB, KO, and FD) are fit by a first-order polynomial. Present day hotspot latitudes are defined by the zero age location on the age progression curves. Dashed lines represent portions of the chain with little to no seamount data. For better comparison, all chains are plotted with the same age-axis and distance-axis scale.

BIBLIOGRAPHY

Andrews, David L., Richard G. Gordon, and Benjamin C. Horner-Johnson. 2006. "Uncertainties in plate reconstructions relative to the hotspots; Pacific-hotspot rotations and uncertainties for the past 68 million years." *Geophys. J. Int.* 166 (2): 939–951.

Austermann, Jacqueline, Zvi Ben-Avraham, Peter Bird, Oliver Heidbach, Gerald Schubert, and Joann M. Stock. 2011. "Quantifying the forces needed for the rapid change of Pacific plate motion at 6 Ma." *Earth and Planetary Science Letters* 307 (3–4): 289–297.

Ballmer, Maxim D, Garrett Ito, Cecily J Wolfe, and Sean C Solomon. 2013. "Double layering of a thermochemical plume in the upper mantle beneath Hawaii." *Earth and Planetary Science Letters* 376:155–164.

Bono, Richard K, John A Tarduno, and Hans-Peter Bunge. 2019. "Hotspot motion caused the Hawaiian-Emperor Bend and LLSVPs are not fixed." *Nature communications* 10 (1): 1–9.

Cande, Steven C. 1976. "A palaeomagnetic pole from Late Cretaceous marine magnetic anomalies in the Pacific." *Geophysical Journal International* 44 (3): 547–566.

Clague, DA. 1996. "The growth and subsidence of the Hawaiian-Emperor volcanic chain." *The origin and evolution of Pacific island biotas, New Guinea to eastern Polynesia: patterns and processes:* 35–50.

Clouard, Valérie, and Alain Bonneville. 2005. "Ages of seamounts, islands, and plateaus on the Pacific plate." *Special Papers-Geological Society of America* 388:71.

Conrad, Clinton P, Bernhard Steinberger, and Trond H Torsvik. 2013. "Stability of active mantle upwelling revealed by net characteristics of plate tectonics." *Nature* 498 (7455): 479–482.

Cox, Allan, and David Engebretson. 1985. "Change in motion of Pacific plate at 5 Myr BP." *Nature* 313 (6002): 472–474.

Doubrovine, Pavel V, Bernhard Steinberger, and Trond H Torsvik. 2012. "Absolute plate motions in a reference frame defined by moving hot spots in the Pacific, Atlantic, and Indian oceans." *Journal of Geophysical Research: Solid Earth* 117 (B9).

Duncan, Robert A, and David A Clague. 1985. "Pacific plate motion recorded by linear volcanic chains." *The ocean basins and margins:* 89–121.

Goldreich, Peter, and Alar Toomre. 1969. "Some remarks on polar wandering." *Journal of Geophysical Research* 74 (10): 2555–2567.

Heaton, DE, and AAP Koppers. 2019. "High-resolution 40Ar/39Ar geochronology of the Louisville Seamounts IODP Expedition 330 drill sites: Implications for the duration of hot spot-related volcanism and age progressions." *Geochemistry, Geophysics, Geosystems* 20 (8): 4073–4102.

Hillier, JK, and AB Watts. 2005. "Relationship between depth and age in the North Pacific Ocean." *Journal of Geophysical Research: Solid Earth* 110 (B2).

Jicha, Brian R, Michael O Garcia, and Paul Wessel. 2018. "Mid-Cenozoic Pacific plate motion change: Implications for the northwest Hawaiian Ridge and circum-Pacific." *Geology* 46 (11): 939–942.

Kono, M. 1980. "Paleomagnetism of DSDP Leg 55 basalts and implications for the tectonics of the Pacific plate." *Initial Reports of the Deep Sea Drilling Project* 55:737–752.

Konrad, Kevin, Anthony AP Koppers, Bernhard Steinberger, Valerie A Finlayson, Jasper G Konter, and Matthew G Jackson. 2018. "On the relative motions of long-lived Pacific mantle plumes." *Nature Communications* 9 (1): 1–8.

Koppers, Anthony AP, Molly D Gowen, Lauren E Colwell, Jeffrey S Gee, Peter F Lonsdale, John J Mahoney, and Robert A Duncan. 2011. "New 40Ar/39Ar age progression for the Louisville hot spot trail and implications for inter–hot spot motion." *Geochemistry, Geophysics, Geosystems* 12 (12).

Koppers, Anthony AP, Jason Phipps Morgan, Jason W Morgan, and Hubert Staudigel. 2001. "Testing the fixed hotspot hypothesis using 40Ar/39Ar age progressions along seamount trails." *Earth and Planetary Science Letters* 185 (3-4): 237–252.

Koppers, Anthony AP, Jamie A Russell, Jed Roberts, Matthew G Jackson, Jasper G Konter, Dawn J Wright, Hubert Staudigel, and Stanley R Hart. 2011. "Age systematics of two young en echelon Samoan volcanic trails." *Geochemistry, Geophysics, Geosystems* 12 (7).

Menke, William. 2018. *Geophysical data analysis: Discrete inverse theory.* Academic press.

Morgan, W Jason. 1971. "Convection plumes in the lower mantle." *Nature* 230 (5288): 42–43.

Müller, R Dietmar, Sabin Zahirovic, Simon E Williams, John Cannon, Maria Seton, Dan J Bower, Michael G Tetley, Christian Heine, Eline Le Breton, Shaofeng Liu, et al. 2019. "A global plate model including lithospheric deformation along major rifts and orogens since the Triassic." *Tectonics* 38 (6): 1884–1907.

O'Connor, John M, Bernhard Steinberger, Marcel Regelous, Anthony AP Koppers, Jan R Wijbrans, Karsten M Haase, Peter Stoffers, Wilfried Jokat, and Dieter Garbe-Schönberg. 2013. "Constraints on past plate and mantle motion from new ages for the Hawaiian-Emperor Seamount Chain." *Geochemistry, Geophysics, Geosystems* 14 (10): 4564–4584.

O'Neill, Craig, Dietmar Müller, and Bernhard Steinberger. 2005. "On the uncertainties in hot spot reconstructions and the significance of moving hot spot reference frames." *Geochemistry, Geophysics, Geosystems* 6 (4).

Parés, Josep M, and Ted C Moore. 2005. "New evidence for the Hawaiian hotspot plume motion since the Eocene." *Earth and Planetary Science Letters* 237 (3-4): 951–959.

Petronotis, Katerina E, Richard G Gordon, and Gary D Acton. 1994. "A 57 Ma Pacific plate palaeomagnetic pole determined from a skewness analysis of crossings of marine magnetic anomaly 25r." *Geophysical Journal International* 118 (3): 529–554.

Pollitz, Fred F. 1986. "Pliocene change in Pacific-plate motion." *Nature* 320 (6064): 738–741.

Sharp, Warren D, and David A Clague. 2006. "50-Ma initiation of Hawaiian-Emperor bend records major change in Pacific plate motion." *Science* 313 (5791): 1281–1284.

Skilbeck, John N, and John A Whitehead. 1978. "Formation of discrete islands in linear island chains." *Nature* 272 (5653): 499–501.

Steinberger, Bernhard. 2000. "Plumes in a convecting mantle: Models and observations for individual hotspots." *Journal of Geophysical Research: Solid Earth* 105 (B5): 11127–11152.

Tarduno, John A, and Rory D Cottrell. 1997. "Paleomagnetic evidence for motion of the Hawaiian hotspot during formation of the Emperor seamounts." *Earth and Planetary Science Letters* 153 (3-4): 171–180.

Tarduno, John A, Robert A Duncan, David W Scholl, Rory D Cottrell, Bernhard Steinberger, Thorvaldur Thordarson, Bryan C Kerr, Clive R Neal, Fred A Frey, Masayuki Torii, et al. 2003. "The Emperor Seamounts: Southward motion of the Hawaiian hotspot plume in Earth's mantle." *Science* 301 (5636): 1064–1069.

Tarduno, John, Hans-Peter Bunge, Norm Sleep, and Ulrich Hansen. 2009. "The bent Hawaiian-Emperor hotspot track: Inheriting the mantle wind." *Science* 324 (5923): 50–53.

Tauxe, Lisa. 2006. *Paleomagnetic principles and practice.* Vol. 17. Springer Science & Business Media.

Tetley, Michael G, Simon E Williams, Michael Gurnis, Nicolas Flament, and R Dietmar Müller. 2019. "Constraining absolute plate motions since the Triassic." *Journal of Geophysical Research: Solid Earth* 124 (7): 7231–7258.

Torsvik, Trond H, Pavel V Doubrovine, Bernhard Steinberger, Carmen Gaina, Wim Spakman, and Mathew Domeier. 2017. "Pacific plate motion change caused the Hawaiian-Emperor Bend." *Nature Communications* 8 (1): 1–12.

Tozer, B, DT Sandwell, WHF Smith, C Olson, JR Beale, and P Wessel. 2019. "Global bathymetry and topography at 15 arc seconds: SRTM15+V2.0." *Earth and Space Sciences* 6 (10): 1847–1864.

Tsai, Victor C, and David J Stevenson. 2007. "Theoretical constraints on true polar wander." *Journal of Geophysical Research: Solid Earth* 112 (B5).

Watts, Anthony Brian. 2001. *Isostasy and Flexure of the Lithosphere.* Cambridge University Press.

Wessel, Paul. 1998. "An empirical method for optimal robust regional-residual separation of geophysical data." *Mathematical Geology* 30 (4): 391–408.

———. 2012. "New Reference Models for Pacific Absolute Plate Motion." In *AGU Fall Meeting Abstracts,* vol. 2012, DI44A–07.

———. 2016. "Regional–residual separation of bathymetry and revised estimates of Hawaii plume flux." *Geophysical Journal International* 204 (2): 932–947.

Wessel, Paul, and Clinton P Conrad. 2019. "Assessing models for Pacific absolute plate and plume motions." *Geochemistry, Geophysics, Geosystems* 20 (12): 6016–6032.

Wessel, Paul, and Loren W Kroenke. 2000. "Ontong Java Plateau and late Neogene changes in Pacific plate motion." *Journal of Geophysical Research: Solid Earth* 105 (B12): 28255–28277.

———. 2007. "Reconciling late Neogene Pacific absolute and relative plate motion changes." *Geochemistry, Geophysics, Geosystems* 8 (8).

———. 2008. "Pacific absolute plate motion since 145 Ma: An assessment of the fixed hot spot hypothesis." *Journal of Geophysical Research: Solid Earth* 113 (B6).

———. 2009. "Observations of geometry and ages constrain relative motion of Hawaii and Louisville plumes." *Earth and Planetary Science Letters* 284 (3-4): 467–472.

Whittaker, Joanne M, Alexey Goncharov, Simon E Williams, R Dietmar Müller, and German Leitchenkov. 2013. "Global sediment thickness data set updated for the Australian-Antarctic Southern Ocean." *Geochemistry, Geophysics, Geosystems* 14 (8): 3297–3305.

Wilson, J Tuzo. 1963. "A possible origin of the Hawaiian Islands." *Canadian Journal of Physics* 41 (6): 863–870.

Winterer, Edward L. 1973. "Sedimentary facies and plate tectonics of equatorial Pacific." *AAPG Bulletin* 57 (2): 265–282.

Woodworth, Daniel, and Richard G Gordon. 2018. "Paleolatitude of the Hawaiian hot spot since 48 Ma: Evidence for a mid-Cenozoic true polar stillstand followed by late Cenozoic true polar wander coincident with Northern Hemisphere glaciation." *Geophysical Research Letters* 45 (21): 11–632.